MAVS Orchestrates a Potent IFN-independent Antiviral Immunity by Preserving Mitochondrial Integrity

Vishal Sah[1,2], Poojitha Sai Potharaju[1,2], Karthika S Nair[1], Prangya Paramita Sahoo[1,2], Abhiram Ravicanti Pooja[1], Debasmita Basu[1], Dixit Tandel[1,2], K.S. Varadarajan[1], Santosh Chauhan[1,2], Anant Bahadur Patel[1,2], and Krishnan Harinivas Harshan[€,1,2]

[1]CSIR-Centre for Cellular and Molecular Biology, Hyderabad, India 500007

[2]Academy for Scientific and Innovative Research (AcSIR), Ghaziabad-201002, India

[€]Correspondence: hkrishnan@ccmb.res.in

Keywords

MAVS, RLR pathway, Interferon-independent, Mitophagy, Mitochondrial dynamics, Viral replication, Host-pathogen interactions, SARS-CoV-2, JEV, DENV, RNA viruses

Abstract

Mitochondria are central to innate antiviral defense, coordinating both energy metabolism and interferon (IFN) responses. While mitochondrial antiviral-signaling protein (MAVS) is well-established for its role in regulating type I and III IFN production, our research unveils a previously unidentified, yet more significant, overarching function: MAVS acts as a protector of mitochondria against mitophagy triggered by viruses and toxins. We show that MAVS is crucial for maintaining TOM complex functionality by influencing the levels of key outer and inner membranes translocases (TOM20/TOM70/TIM23), and the spatial distribution/organization between TOM20:TOM70 in mitochondria. Disruptions to these features caused by MAVS loss, likely compromise mitochondrial protein import, leading to increased mitochondrial PINK1 stabilization and its phosphorylation, and elevated mitophagy. These changes resulted in significantly compromised mitochondrial bioenergetics, with implications on immune response. Notably, MAVS supplementation not only mitigated mitophagy in MAVS KO cells, but also conferred protection against mitophagy induced by viruses (SARS-CoV-2, and Japanese encephalitis virus (JEV)), and mitotoxins, indicating its broad protective role against mitophagy. Furthermore, we reveal that MAVS-mediated mitochondrial stabilization elicits a robust antiviral immunity against mitophagy-inducing viruses without engaging IFN- and NF-κB pathways, underscoring the significance of this mechanism in host antiviral defense. The redefined role of MAVS as a critical mitochondrial stabilizer has implications extending beyond its broad antiviral immunity, which involves both IFN-dependent and IFN-independent mechanisms, to encompass various pathological conditions involving mitochondrial dysfunction.

INTRODUCTION

RNA viruses are recognized by cytosolic RLRs, RIG-I and MDA5 (*1, 2*), which initiate antiviral signaling through MAVS located on the outer mitochondrial and peroxisomal membranes (*3, 4*) MAVS activation triggers the formation of a signaling complex that ultimately leads to the production of type I and III IFNs (*5*). Functional MAVS requires its N-terminal CARD domain for its oligomerization and its C-terminal TM domain for its anchoring to mitochondrial and peroxisomal outer membrane (*3, 4*). As MAVS oligomerization via its CARD domain is a key event in this regulation, it is often

targeted by viruses to inactivate IFN-mediated innate immune response (*6-9*). Hyper-activation of MAVS has been implicated in autoimmune condition Systemic Lupus erythematosus (SLE) (*10, 11*). While MAVS is well-known for its role in IFN induction, its broader impact on mitochondrial integrity and its downstream consequences remain largely unexplored.

Mitochondria are critical organelles in the innate antiviral response, serving not only as energy producers but also as platforms for immune signaling. Mitochondria–ER contact sites (MERCs) are essential for MAVS-mediated downstream signaling (*12, 13*), and mitochondria host other innate immune sensors such as the NLRP3 Inflammasome (*14, 15*). Viruses exploit this centrality by disrupting mitochondrial dynamics and homeostasis—inducing fission, triggering mitophagy (*8, 16, 17*), and impairing MAVS signaling—to subvert host immunity (*18, 19*). In parallel, mitochondrial targeting enables viruses to reprogram host metabolism toward glycolysis, which both suppresses antiviral responses and supports viral replication by supplying biosynthetic intermediates (*20-23*). SARS-CoV-2 (CoV-2) and other viruses upregulate glycolysis to meet their energy demands, and glycolytic inhibition has been shown to significantly reduce viral replication (*24-26*). In this context, the integrity of mitochondrial protein import becomes critical. As over 99% of mitochondrial proteins are nuclear-encoded, their import depends on the coordinated action of the TOM and TIM complexes (*27, 28*). The TOM complex, comprising TOM40 and receptors like TOM20 and TOM70, initiates precursor translocation across the outer membrane, followed by TIM23-mediated transport across the inner membrane (*29*). Disruption of this import system compromises mitochondrial homeostasis, impairs respiration, and activates stress responses such as PINK1/Parkin-dependent mitophagy. Thus, maintaining mitochondrial import fidelity is essential for supporting antiviral signaling and metabolic resilience during infection.

CoV-2 profoundly delays the innate immune response by intercepting both upstream and downstream of MAVS (*30-36*). Studies have demonstrated that earlier CoV-2 variants are susceptible to IFN and RLR activation, but the later variants had evolved mechanisms to overcome this susceptibility (*37, 38*). Interestingly, CoV-2 also promotes mitophagy, similar to JEV (*39*). In contrast, Dengue virus (DENV) do not

cause mitophagy (*40*), suggesting a complex relationship between viruses and mitochondrial homeostasis.

Here, we demonstrate that MAVS plays a critical role in safeguarding mitochondria, extending beyond its canonical function in IFN signaling. We show that MAVS has important roles maintaining the TOM complex distribution and organization in mitochondria, which is directly linked to the mitochondrial homeostasis. MAVS loss resulted in increased PINK1-mediated mitophagy, thereby seriously compromising the antiviral immunity. We also identify a potent antiviral immunity operating independent of IFN- and NF-κB pathways directly linked to MAVS-mediated mitochondrial stabilization. Our findings establish mitochondrial protection as the core function of MAVS, which in turn orchestrates a broad antiviral response through both IFN-dependent and independent mechanisms.

RESULTS

CoV-2 disrupts MAVS aggregation and evades the RLR-mediated Immunity

Previous studies have shown that CoV-2 proteins delay the RLR response (*41, 42*). We independently confirmed this delay in Caco2 and Huh7 cells infected with a variant isolate B.1.1.8, which was used throughout this study. Both cell lines supported robust CoV-2 replication (Figures S1 A-C). Consistent with our prior findings in Caco2 cells (*37*), Huh7 also exhibited delayed IRF3 phosphorylation, *IFNB1* transactivation, and STAT1 phosphorylation (Figures S1 D&E) until 48 hpi. Notably, MAVS levels remained unchanged across these conditions (Figures S1 C, D, F, and G). This delayed RLR activation was specific to SARS-CoV-2, contrasting with the quicker activation observed in flavivirus infections like JEV and DENV (*43, 44*) (Figure S1H). SDD-AGE analysis revealed a reduced MAVS aggregation in CoV-2-infected cells starting at 12 and 24 hpi, recovering by 48 hpi (Figure 1A). We further corroborated this finding using confocal microscopy. MAVS, which is diffusely distributed, aggregates and forms distinct puncta-like structures on the outer mitochondrial surface upon activation (*45*) (Figure S1I). As expected, MAVS formed strong puncta in poly(I:C)-transfected cells (Figure S1J), but not upon ΔCARD MAVS transfection, displaying a higher Pearson coefficient for colocalization with mitochondria (Figure S1K). In CoV-2-infected cells, MAVS showed weaker aggregation and stronger mitochondrial colocalization at 12 and 24 hpi but exhibited

puncta formation by 48 hpi compared to mock controls (Figures 1B, C), mirroring the SDD-AGE results. In contrast, both JEV and DENV infections resulted in strong MAVS aggregation by 24 hpi (Figures S1 L&M). The temporal correlation between recovered MAVS aggregation and increased IRF3 phosphorylation at 48 hpi strongly suggests that CoV-2-mediated regulation of MAVS aggregation is a key mechanism underlying the observed delay in the IFN response.

Exogenous RLR supplementation activates type-I IFN production independent of ligand binding (*1, 2*). We tested whether this could overcome CoV-2-mediated RLR suppression in Huh7 cells, which showed strong permissivity to CoV-2 (*46*) (Figures S1 A&B), superior transfection efficiency (Figure S1N) and imaging suitability. Cells were transfected prior to infection, and analyzed at 24 hpi (Figure S1O), a time point where IFN activation is clearly absent, allowing for an unbiased evaluation of overexpression effects. Overexpression of RIG-I, MDA5, and TBK1 strongly induced IRF3 phosphorylation; however, it failed to activate *IFNB1* transcription, and did not restrict CoV-2 replication (Figures 1 D–H). In contrast, these same factors robustly induced *IFNB1* expression in uninfected cells (Figures S1 P–S), confirming that SARS-CoV-2 infection blocks type I IFN production downstream of IRF3 activation, consistent with previous reports (*33, 47*). Supporting this, the constitutively active S396E IRF3 also failed to induce *IFNB1* or restrict viral replication in infected cells (Figures 1 I–K) despite strongly activating *IFNB1* in naïve cells (Figures S1 T&U). Collectively, these findings demonstrate that CoV-2 disrupts MAVS aggregation and IRF3-mediated IFN induction, effectively neutralizing the RLR-driven IFN dependent antiviral response.

Functional MAVS can efficiently restrict CoV-2

Given MAVS's central role in the RLR pathway, we next tested whether its supplementation could restrict CoV-2. MAVS supplementation triggers its oligomerization resulting in IFN induction (*3, 48*). Interestingly, FL-MAVS, but not its ΔCARD variant, could significantly reduce CoV-2 infectious titers (Figures 2 A&B) and dsRNA levels (Figures 2 C&D) compared to control cells transfected with an empty vector. Similar results were observed in Caco2 cultures (Figures S 2 A&B). FL-MAVS aggregates localized predominantly on mitochondria, but not on

peroxisomes, suggesting that the viral suppressive effects by MAVS is mediated through mitochondria (Figure S 2C&D).

To further validate these findings, we generated MAVS KO Huh7 cells, which showed markedly higher CoV-2 permissivity than WT cells (Figures 2 E–H). FL-MAVS supplementation, but not its ΔCARD variant, suppressed CoV-2 infection also in the MAVS KO cells, measured by dsRNA levels and viral titers, confirming the requirement of CARD domain and MAVS aggregation (Figures 2 I–K). We extended this study to A549 cells, known for low ACE2 expression and limited CoV-2 replication (*46, 49*) (Figure 2L). Surprisingly, MAVS KO A549 cells supported robust SARS-CoV-2 replication, reaching titers comparable to highly permissive Caco2 and Huh7 cells (Figures 2 M&N, Figure S1B). While WT A549 cells effectively cleared the infection over time, high viral titers persisted in MAVS KO A549 cells until 72 hpi. FL-MAVS supplementation significantly lowered CoV-2 titers in MAVS KO A549 cells, similar to our observation in Huh7 (Figures S2E&F). We further tested this in MAVS KO mouse embryonic fibroblasts (MEFs). Despite mice being non-permissive to CoV-2(*50*), MEFs surprisingly supported robust infection (Figures 2 O&P). Consistent with MAVS KO A549 cells, viral replication declined in WT MEFs over time, whereas MAVS KO MEFs sustained high titers. These findings highlight two key points: (i) functional MAVS effectively restricts CoV-2, and (ii) MAVS supplementation can counteract CoV-2-mediated MAVS inactivation, providing a potent antiviral mechanism.

The antiviral effect of MAVS against CoV-2 is independent of type I and type III IFN, and NF-κB signaling

Although FL-MAVS suppressed CoV-2 replication, we interestingly noticed a total absence of any increase in IRF3 phosphorylation or type I IFN induction (Figures 3 A-D, S2G-I). The effect was specific to CoV-2, since MAVS activated both responses during JEV and DENV infections (Figures S2 N-S), suggesting an IFN-independent mechanism. In contrast, MAVS supplementation in naive cells led to strong IRF3 phosphorylation and type I IFN induction (Figures S2 J-M). To understand this better, we examined MAVS's potential to restrict CoV-2 Alpha and Delta variants, both known to resist RLR activation and IFN-α treatment (*37*). MAVS effectively suppressed both variants (Figure 3E), further supporting the type I IFN-independent

nature of this restriction. Interestingly, MAVS supplementation led to notable induction of *IFNL1* expression in both naive and CoV-2 infected cells, indicating its potential role in CoV-2 restriction (Figure S2T, Figure 3F). However, treatment with IFN-λ failed to significantly suppress CoV-2, indicating that MAVS-mediated restriction is independent of both type I and type III IFN signaling (Figures 3 G-I). If such a mechanism exists, we reasoned that it should supplement the IFN-mediated suppression. Indeed, combining MAVS supplementation with IFN-α treatment resulted in significantly stronger CoV-2 suppression than either treatment alone (Figures 3 J&K). Further, MAVS-mediated CoV-2 suppression persisted despite JAK inhibition by Baricitinib (Figures 3 L&M) or type-I IFN neutralization by neutralizing antibodies (Figures 3 N&O). Since Baricitinib blocks JAK signaling, needed for both type I- and III IFN signaling, this finding rules out the involvement of either of these IFN signaling in this process. Finally, we developed a MAVS:IFNAR1 double knockout (DKO) mouse model to further investigate this observation (Figure S2U). Consistent with the findings so far, mMAVS supplementation in DKO MEFs significantly reduced CoV-2 titers (Figures 3 P&Q). Since MAVS also signals through NF-κB, we investigated whether NF-κB was involved in this process. However, inhibiting NF-κB with BAY11-7082 did not reverse MAVS-mediated suppression of CoV-2 (Figures 3 R&S), ruling out the NF-κB pathway's involvement. Together, these findings demonstrate that MAVS activates a powerful but yet unidentified mechanism to clear CoV-2, independent of type I and III interferons as well as NF-κB.

MAVS regulates a broader transcriptional landscape, distinct from IFN

To explore the IFN-independent antiviral programs mediated by MAVS, we conducted transcriptomic analysis of Huh7 cells overexpressing MAVS or treated with IFN-α under both uninfected and CoV-2 infected conditions (Figures S1O, S3A). Transcriptome profiles of CoV-2 infected or uninfected cultures overexpressing MAVS or treated with IFN-α were normalized against those from the empty vector-transfected or vehicle-treated. The results revealed a striking contrast: while IFN induced a focused transcriptional response, MAVS activated a broader transcriptional program (Figure 4A). IFN regulated 232 DEGs in Huh7 cells, increasing to 332 upon CoV-2 infection, whereas MAVS influenced 1,748 DEGs,

rising to 2,407 post-infection, with minimal gene overlap (Figures 4 B&C). GO analysis of the common DEGs highlighted enrichment in antiviral pathways (Figure S3B). Notably, only ~ 6% of MAVS-regulated DEGs were linked to innate immunity, compared to ~ 26% for IFN (Figure S3C). While there was substantial overlap among the ISGs, each condition also uniquely regulated specific subsets of ISGs (Figures S3 D–G). Importantly, MAVS overexpression regulated a larger subset of ISGs compared to IFN-α treatment. These findings underscore the broader regulatory role of MAVS in antiviral defense, extending beyond its established function in IFN induction.

Given MAVS's mitochondrial localization, we examined whether it engages specific mitochondrial pathways beyond its established antiviral role. Enrichment analysis of MAVS overexpression transcriptome revealed mitochondria-associated pathways related to oxidative stress, membrane permeability, and organization (Figure 4D). Among them, upregulation of genes such as *TOMM40*, *CHCHD10*, and *PPIF* suggested a role for MAVS in maintaining enhanced mitochondrial stability (*51-53*), while *PDE2A*, *PLA2G2A*, and *RSAD2* highlighted MAVS's broader metabolic regulatory role (*54-56*) (Figures 4 E&F).

We next analyzed transcriptomes of WT and MAVS KO MEFs across infection states and time points, focusing broadly on mitochondrial processes associated with MAVS loss. Transcriptomes were normalized to their corresponding WT controls at matching time points. As expected, MAVS KO MEFs exhibited impaired antiviral responses and increased mitochondrial dysfunction during SARS-CoV-2 infection (Figure 4G). As observed in the MAVS overexpression system, GO analysis of MAVS KO transcriptome showed upregulation of terms related to mitochondrial fission, apoptosis, and ROS metabolism. Notably, *Prkn*, *Ppargc1a*, and *Dcn* were upregulated in MAVS KO MEFs (Figure 4H), alongside pro-apoptotic genes *Pmaip1* and *Cdkn2a*, indicating mitochondrial destabilization and reduced ATP production (Figure 4I). Further, downregulation of ATP synthesis, oxidative phosphorylation and mitochondrial transport pathways further pointed to mitochondrial dysfunction (Figures 4J, S3H). Specifically, reduced expression of NADH dehydrogenase subunits (*ND1*, *ND2, ND4, ND5, ND6*) and ATP synthase subunits (*ATP6, ATP8*)- all mitochondrial encoded genes- suggested a reduced mitochondrial gene expression,

leading to a possibly compromised energy production upon the loss of MAVS (Figures 4 K&L). Additionally, downregulation of *Tomm70A*, *Timm23*, and *Timm13* would likely have disrupted mitochondrial protein transport and membrane integrity, exacerbating mitochondrial instability (Figures 4 M&N).

It may be noted that our study covered two distinct cell lineages and two distinct mammalian species. To investigate the core genes that are regulated by MAVS across these two variables, we performed a homolog mapping between MAVS-overexpressing Huh7 cells and MAVS-knockout MEFs. Several genes including a few IFN-stimulated genes (ISGs) such as *Ifih1*, *Ifih5*, and *Oas1a* represented this overlapping list (Figure S3I). This list also featured *Prkn1*, an important gene regulating mitophagy, and *Cmpk2*, a gene important in mitochondrial health (*57*). These findings indicate that MAVS positively regulates mitochondrial stability through multiple distinct programs.

CoV-2 disrupts mitochondrial homeostasis and causes mitophagy that benefits its replication

Given that our RNA-seq data identified several mitochondrial processes regulated by MAVS, we sought to find out whether these processes underlie the IFN-independent antiviral state. Preliminary observations suggested a significant mitochondrial network disruption with CoV-2 infection (Figure 1B). Other reports have shown that CoV-2 induced incomplete mitophagy that enhanced its replication (*39*). We independently verified this observation, finding significant, and progressively intensifying mitochondrial fragmentation (Figures 5 A-B). The infection was characterized by severely depolarised mitochondria (Figures 5 C-D), leading to considerable loss in mitochondrial mass (Figures S4 A-B). Markedly higher levels of LC3 in CoV-2 infected cells indicated mitophagy induction (Figure S4C) that was further confirmed by a mito-GFP-RFP reporter-based assay (Figures 5 E-F). Coupled with a strong increase in PINK1 localization to mitochondria and its phosphorylation, this finding demonstrated a PINK1-Parkin mediated mitophagy induction by CoV-2 (Figures 5 G-J). In CoV-2-infected cells, mitochondria aggregated into giant clumps, which were distinct from those observed in JEV-infected cells, where mitophagy is a known response (*58*) (Figures S4 D-I). Super resolution microscopy identified the giant clumps as convoluted mitochondrial

aggregates (Figures S4 J-K). Interestingly, these clumps exhibited stronger mitophagic signals and were largely devoid of MAVS (Figure 5K). However, a significant subset still retained MAVS, suggesting that these intact mitochondria may be actively coordinating signaling modules for IFN production observed at 48 hpi. Contrasting CoV-2 and JEV, DENV induced mitochondrial elongation without triggering mitophagy (Figure S4D-I), consistent with previous reports (*40, 59*). Assessment of CoV-2 replication upon CCCP-induced mitophagy revealed markedly enhanced CoV-2 replication, suggesting that CoV-2-driven mitophagy facilitates its replication (Figures 5 L-O, Figures S4 L&M). Consistent with previous findings, mitophagy enhanced JEV replication but hindered DENV replication (Figures S4 N-Q). These results confirmed that the induction of mitophagy by CoV-2 and JEV is beneficial to their propagation.

MAVS deficiency predisposes mitochondria to mitophagy and dysfunction

Having confirmed the induction of mitophagy during CoV-2 infection, we investigated whether MAVS plays a role in preserving mitochondrial integrity. We interestingly observed that mitochondria in MAVS KO Huh7 cells and MEFs were strikingly smaller in size compared to those in wild-type (WT) cells, suggesting that MAVS loss compromises mitochondrial structure (Figures 6 A&B & Figures S5A-C). Further analysis revealed that mitochondria in MAVS KO cells exhibited significantly lower membrane potential (measured by JC1 staining), lower mitochondrial count, and reduced mitochondrial mass (measured by Mitotracker Green) (Figures S5 D-J), suggesting that MAVS plays an important role in maintaining the mitochondrial membrane integrity. Notably, MAVS KO cells exhibited elevated levels of mitophagy as compared to the WT cells (Figures 6 C&D, Figures S5 K&L). Consistent with these findings and in agreement with our RNA-seq data, MAVS KO cells exhibited a significant decline in mitochondrial oxygen consumption rate (OCR) and respiratory capacity (Figures 6 E&F, Figures S5 M&N, Figure 4L), confirming that MAVS loss not only disrupts mitochondrial structure but also impairs its metabolic function. As a potential outcome, MAVS KO cells displayed markedly slower growth rates (Figure S5O). To determine the specificity of MAVS function, we examined whether MAVS supplementation could restore mitochondrial integrity. Full-length MAVS (FL-MAVS) supplementation, but not the ΔCARD variant, restored normal elongated mitochondrial morphology in MAVS KO cells (Figures 6 G&H) and further promoted

mitochondrial elongation in WT cells (Figures S5 P&Q). This stabilization was accompanied by restored mitochondrial respiration in MAVS KO cells (Figures 6 I&J) and enhanced respiration in WT cells (Figures S5 R&S). These results establish that MAVS deficiency renders mitochondria highly susceptible to fragmentation and mitophagy, thereby compromising their function. Given that MAVS was able to suppress virus-induced mitophagy, we next assessed whether MAVS supplementation could protect mitochondria from toxin-induced mitophagy. FL-MAVS effectively suppressed CCCP-induced mitochondrial fragmentation (Figures 6 K&L), depolarisation (Figures S5 T&U), and mitophagy (Figures 6 M&N). These findings position MAVS as a critical protector of mitochondrial integrity under both basal and stress conditions.

MAVS supports mitochondrial protein import machinery/complex and restricts PINK1-mediated mitophagy

Prompted by the reported interactions of MAVS with TOM70 and with PINK1 (*60, 61*), we hypothesized that MAVS could be potentially influencing the mitochondrial protein trafficking complex by influencing TOM:PINK1 stabilization. PINK1 stabilization on mitochondrial membrane, an early event in PINK-dependent mitophagy is mediated through TOM complex (*62*). Consistent with our RNA-seq data implicating MAVS in mitochondrial protein import (Figures 4M–N), we observed a marked reduction in TIM23, TOM20, and TOM70 protein levels in MAVS KO Huh7 cells (Figures 7A–B). The reduction in TOM70 is particularly notable, given its previously demonstrated interaction with MAVS and its role in IRF3 signaling (*60*).

To evaluate whether MAVS loss alters the distribution of import receptors on mitochondria, we next quantified TOM20 and TOM70 receptor density. Importantly, instead of using mean fluorescence intensity (MFI)—which would be confounded by the reduced mitochondrial number in MAVS KO cells—we consciously measured TOM20 and TOM70 density normalized to total mitochondrial area. This approach allowed for an unbiased comparison of receptor distribution independent of mitochondrial content. We observed a substantial reduction in TOM20 and TOM70 density on the mitochondrial surface in MAVS-deficient cells (Figures 7 C–E).

To further probe receptor module integrity, we analyzed the spatial organization of TOM20 and TOM70. Since TOM20–TOM70 interactions are transient and their

spatial proximity is critical for efficient precursor delivery to TOM40, we measured the density of TOM20:TOM70 intersections and their centroid-to-centroid distance on the mitochondrial surface. Notably, instead of relying on traditional colocalization coefficients—which can be biased by variations in signal intensity and mitochondrial abundance—we quantified intersection density as a more robust and intensity-independent metric. This approach ensures that the observed changes reflect genuine alterations in receptor organization rather than artifacts from reduced mitochondrial content or fluorescence intensity in MAVS-deficient cells. Using this method, we found that MAVS-deficient cells exhibited a significant reduction in TOM20:TOM70 intersection density, along with an increased spatial separation between TOM20 and TOM70 (Figures 7 F–H). These results suggest that MAVS is critical for maintaining receptor alignment in the TOM complex, thereby potentially influencing the import efficiency across mitochondrial membranes.

Consistent with altered organization of the import machinery, MAVS KO cells exhibited increased PINK1 accumulation and phosphorylation at the mitochondrial surface (Figures 7I–L), indicative of mitophagy initiation. Full-length MAVS supplementation efficiently suppressed CCCP- and MPTP-induced PINK1 phosphorylation and reduced LC3-mitochondrial association (Figures 7M–N, Figures S5 V–Z). Collectively, these findings demonstrate that MAVS safeguards mitochondrial protein trafficking by stabilizing translocase organization and preventing aberrant PINK1 activation.

MAVS protects mitochondria from virus-induced damage and mediates IFN-independent antiviral immunity

We next investigated whether functional MAVS could prevent the mitochondrial damage induced by CoV-2. Similar to its protective effects against mitotoxins, overexpression of full-length MAVS (FL-MAVS), but not the ΔCARD MAVS variant, prevented CoV-2-induced mitochondrial fragmentation and promoted mitochondrial elongation (Figures 8 A&B, Figure S6A). This was accompanied by an increase in mitochondrial mass (Figures S6 B&C), reduced mitochondrial depolarization (Figures S6 D&E), and diminished LC3 association with mitochondria (Figure S6F), indicating that MAVS protects against CoV-2-mediated mitochondrial damage. A Mito-GFP-RFP reporter assay further confirmed that MAVS supplementation effectively

prevented mitophagy following CoV-2 infection (Figures 8 C&D). Additionally, a significant reduction in PINK1 phosphorylation in CoV-2-infected cells supplemented with MAVS, similar to the observations in the mitotoxins study, demonstrated that functional MAVS suppresses PINK1 phosphorylation and mitigates mitophagy (Figures 8 E&F, Figures S6 G-I). A comparable reduction in PINK1 phosphorylation was also observed in MAVS KO cells upon MAVS supplementation (Figures 8 G&H, Figures S6 G-I). Consistent with its role in mitochondrial stabilization that we established in the previous sections, MAVS supplementation in CoV-2-infected cells led to a reduction in glycolytic metabolite levels and a decrease in ATP synthesis rate, suggesting a reversal of the virus-induced metabolic shift (Figures 8 I&J). Collectively, these findings demonstrate that MAVS activation upon its supplementation effectively prevents CoV-2-induced mitochondrial damage, mitigates the associated metabolic alterations, and thereby restricts CoV-2 replication.

We sought to understand if MAVS's mito protection is broadly antiviral by testing effects on other viruses. Similar to our findings with CoV-2, MAVS supplementation effectively reduced mitochondrial depolarization caused by JEV, confirming its ability to safeguard mitochondria from virus-induced damage (Figures S 6J&K) and mitophagy (Figures S6 L&M). In contrast, no changes in mitochondrial potential were observed following DENV infection, known to not induce mitophagy (Figures S6 J&K). Given that JEV and DENV impact mitochondria differently, we next investigated whether MAVS could still exert antiviral effects against them in the absence of IFN signaling. As in CoV-2, inhibition of IFN signaling had no notable impact on MAVS-mediated suppression of JEV (Figures S6 N&O). Further, MAVS could significantly suppress JEV infection in MAVS-/-, IFNAR1-/- DKO cells, confirming that mitochondrial stabilization by MAVS triggers a robust, IFN-independent antiviral mechanism targeted against mitophagy-inducing viruses (Figure S6P). In contrast, MAVS-mediated suppression of DENV was completely abolished upon IFN inhibition (Figures S6 Q&R), indicating that the IFN-independent antiviral function of MAVS is ineffective against viruses that do not induce mitophagy. These results establish that MAVS-mediated IFN-independent antiviral immunity is directly linked to its role in mitochondrial stabilization. By protecting mitochondria

from virus-induced mitophagy, MAVS provides a crucial antiviral defense specifically against mitophagy-inducing viruses.

MAVS-mediated mitochondrial safeguarding is type I IFN-independent

Thus far, we have demonstrated that MAVS restricts CoV-2 replication in an IFN-independent manner and plays a crucial role in protecting mitochondria from mitophagy. To determine whether this mitochondrial protection is also IFN-independent, we first tested whether IFN could mimic the mitochondrial-stabilizing effects of MAVS. While IFN-α treatment induced mitochondrial elongation in Huh7 cells, it failed to do so in MAVS KO cells, indicating that IFN-driven mitochondrial elongation is a consequence of MAVS activation rather than a direct effect of IFN itself (Figures 8 K&L).

To further validate this finding, we examined MAVS/IFNAR1 double-knockout (DKO) MEFs, where we had previously demonstrated the IFN-independent nature of MAVS-mediated CoV-2 suppression (Figures 3 O&P). Consistent with this, mMAVS supplementation in these DKO cells also promoted mitochondrial elongation, confirming that MAVS protects mitochondria without engaging IFN signaling (Figures 8 M&N). Additionally, IFN-α provided only modest rescue against mitochondrial fragmentation, depolarization, and mitophagy induced by CCCP (Figures S7 A-F), unlike MAVS, which conferred a much stronger protective effect (Figures 6 K-N & Figures S5 T&U). Similarly, IFN-α failed to restore mitochondrial mass in CoV-2 infected cells, prevent mitochondrial depolarization, or mitigate mitophagy (Figures S7 G-J, Figures 8 O&P). These findings indicate that IFN was unable to sufficiently activate MAVS under these conditions to rescue mitochondrial damage. Based on these observations, we propose a model in which MAVS functions as a central regulator of mitochondrial homeostasis, supporting both IFN-dependent and IFN-independent antiviral responses (Figure 8Q). Together, our results establish that MAVS is critical for preserving mitochondrial integrity during viral infection, and that this protective role is crucial for maintaining the antiviral state upon viral infection.

DISCUSSION

Our study reveals a novel and critical role for the mitochondrial antiviral signaling protein (MAVS) that extends beyond its known involvement in interferon (IFN)

production. We have discovered that MAVS is essential for preserving the structural integrity and homeostasis of mitochondria. We also provide compelling evidence to link this function of MAVS to a potent antiviral immunity that operates independent of IFN. Considering the established importance of mitochondria in the conventional IFN-mediated antiviral pathways, our study positions MAVS as a central orchestrator of cellular defense against viral threats. By actively maintaining mitochondrial health, MAVS empowers a comprehensive antiviral program, effectively coordinating both the well-characterized IFN/NF-κB induction pathways and those that operate independent of them.

Mitochondria are crucial for energy metabolism and for initiating/amplifying antiviral signaling, acting as platforms for complex assembly and signaling molecule generation like mtROS (*63*). Viruses frequently target mitochondria to disrupt these processes, suppressing immunity and reprogramming metabolism for replication. For example, viral induction of mitochondrial fragmentation and mitophagy aids immune evasion and viral propagation (*16*). In the CoV-2 infection model, MAVS aggregation was suppressed and mitophagy was activated. Interestingly, CoV-2 infection systems were ideal to facilitate our findings since it offered an IFN-free natural set up for up to 24 hpi. The IFN-independent antiviral immunity was extensively confirmed in multiple systems including MAVS:IFNAR1 DKO, and inhibition-based assays. Strikingly, similar results were reproduced in JEV infection (belonging to *Flaviviridae* family and distinct from CoV-2) another mitophagy-inducing virus. Conversely, DENV, known to induce mitochondrial elongation and avoid mitophagy, was unaffected by this IFN-independent arm. Using these models, we unambiguously demonstrate that MAVS's critical crucial role in protecting mitochondria from viral-induced damage, arguing that this function is indispensable for its coordination of cellular antiviral defense. This essential role naturally positions MAVS as a strategic target for viruses seeking cellular control.

Previous studies linked MAVS to mitochondrial dynamics and IFN production (*45, 64-69*). There is also evidence in literature about involvement of MAVS in autophagic processes (*70*). Although viral strategies often exploit mitophagy to undermine MAVS signaling, the intrinsic role of MAVS in directly, maintaining mitochondrial homeostasis has received comparatively little attention. While non-canonical

functions exist for specific conditions (*71, 72*), our study significantly expands this view. We demonstrate a broader role for MAVS in safeguarding mitochondrial integrity against a diverse array of mitophagic triggers, including viral infections and pharmacological mitotoxins like CCCP and MPTP. Importantly, we offer potential mechanistic insights into how MAVS regulates key mitochondrial protein trafficking, thereby controlling mitophagy. This protective function is critical for maintaining cellular homeostasis and a robust antiviral defense, establishing MAVS as a key guardian of mitochondrial health at the host-pathogen interface.

Our findings reveal a novel role for MAVS in regulating PINK1-dependent mitophagy through the stabilization of the TOM complex. MAVS's reported interaction with key mitochondrial proteins, including TOM70 and Parkin is likely influencing both mitochondrial protein import and mitophagy regulation (*60, 73*). TOM70, a crucial component of the TOM complex responsible for the trafficking of mitochondrial preproteins, not only supports protein import but also modulates IRF3 signaling (*60*), positioning MAVS as a critical link between mitochondrial integrity and immune activation. Within the TOM complex on the mitochondrial outer membrane, the transient association and spatial proximity of TOM20 and TOM70 are known to be critical for efficient precursor delivery to the central channel, TOM40 (*74*). Our observation that MAVS loss leads to a reduced expression of TOM20, TOM70, and TIM23 strongly suggests that MAVS can directly influence the assembly and stability of translocase complexes by regulating the levels of their individual components. The observed reduction in TIM23 expression aligns with expectations, given its dependence on mitochondrial membrane potential (*75, 76*), a parameter we've previously demonstrated to be significantly compromised in MAVS KO models. However, MAVS also appears to impact TOM complex functionality by modulating the spatial dynamics between TOM20 and TOM70 receptor subunits. We employed quantitative image analysis, measuring both the number of molecular intersections and the centroid-to-centroid distance between neighbouring TOM20 and TOM70 molecules, to assess their transient association, employing similar methodologies to those previously reported (*77, 78*). Given the established link between impaired mitochondrial protein trafficking and the initiation of mitophagy via PINK1 stabilization and phosphorylation, our data support a model wherein MAVS maintains mitochondrial proteostasis by ensuring the stability and functionality of the

import machinery. However, future live-cell import assays will be crucial to definitively establish a causal relationship between MAVS-mediated TOM complex stabilization and efficient protein import, thereby preventing aberrant mitophagy.

While IFN-independent antiviral immunity is a recognized phenomenon, our findings present a novel perspective on its potential mechanisms. We reasoned that common non-specific antiviral agents like mtROS are unlikely mediators in our model. This is because mtROS generation typically requires mitochondrial damage (*79*), whereas our data indicates that MAVS stabilizes mitochondria. Similarly, the NLRP3 Inflammasome pathway, often dependent on ROS signaling (*80*), is also an improbable candidate. Furthermore, the cGAS/STING pathway, a key inducer of type I IFN production, can be excluded given our focus on IFN-independent immunity. Instead, we propose a compelling hypothesis: the observed IFN-independent antiviral activity of MAVS may stem from the restoration of a more physiological metabolic state resulting from mitochondrial stabilization. It is well-established that viral infection often drives a metabolic shift in host cells from oxidative phosphorylation (OXPHOS) to glycolysis, a state that favors robust viral replication (*81*), potentially due to destabilized mitochondria. Our demonstration that MAVS-mediated mitochondrial stabilization enhances mitochondrial respiratory capacity strongly suggests that metabolic rehabilitation could be a critical player in this process. Intriguingly, it remains an open question whether this metabolic reprogramming alone is sufficient to suppress mitophagy, or if it acts synergistically with MAVS's established roles in mitochondrial protein import and dynamics to exert its antiviral effects.

Our findings significantly advance our understanding of the intricate relationship between mitochondrial dynamics, innate antiviral immunity, and viral pathogenesis. This study positions MAVS beyond its established role as a signaling hub, revealing its multifaceted function as a key regulator of mitochondrial architecture, protein import machinery, and cellular metabolism—all critical determinants of a robust antiviral response. The vulnerability of MAVS to viral manipulation underscores its central importance: by targeting MAVS, viruses can effectively compromise mitochondrial integrity, dampen host immune defenses, and even commandeer cellular metabolic pathways to facilitate their own replication. This highlights MAVS

as a compelling therapeutic target for antiviral strategies aimed at preserving mitochondrial homeostasis and enhancing intrinsic host defense mechanisms. Furthermore, the implications of our observations extend beyond the realm of viral infection. The mitochondrial disruptions we observed—fragmentation, impaired protein import, and the activation of PINK1-dependent mitophagy—are not exclusive to viral stress. These same cellular hallmarks are also prominent features of neurodegenerative disorders, notably Parkinson's disease. This intriguing parallel raises the possibility that MAVS, as a central regulator of mitochondrial health in the context of viral infection, may also represent a potential therapeutic avenue for diseases characterized by underlying mitochondrial dysfunction.

Our findings highlight critical unanswered questions at the intersection of mitochondrial membrane integrity and antiviral immunity. A key area for future research is elucidating the regulatory mechanisms by which MAVS influences the spatial organization of TOM complexes on the mitochondrial outer membrane. Given that MAVS aggregation leads to the formation of specialized mitochondrial foci, it is plausible that these domains also concentrate TOM complexes in their vicinity. Supporting this idea, MAVS aggregation sites are reported to overlap with MAMs, crucial platforms for IFN production (*12*). Furthermore, the established role of TOM70 in IRF3 regulation underscores a potential link between TOM complexes and antiviral signaling. Finally, a comprehensive understanding of the post-translational modifications governing MAVS function in antiviral immunity is essential. Future investigations into these areas promise to yield deeper insights into the intricate regulation of mitochondrial membrane trafficking and the maintenance of its integrity.

MATERIALS AND METHODS

Antibodies

MDA-5 (Cat # 5321), RIG-I (Cat #3743), Human MAVS (Cat #24930), Rodent MAVS (Cat #4983), Phospho IRF-3 (Cat #4947), IRF3 (Cat #11904), Phospho-STAT1 (Cat #14994), STAT1 (Cat #9167), IFIT1 (Cat #14769), Phospho P65 (Cat #3033), P65 (Cat #8242), HA-tag (Cat #3724 and #2367), LC3 A/B (Cat #12741), TOM70 (Cat #65619), TOM20 (Cat #42406) were purchased from Cell Signaling Technologies (CST). TIM23 (Cat #sc-514463) and TOM40 (Cat #sc-365467) was from Santa Cruz

Biotechnology. JEV NS1 (Cat #GT1410) and DENV NS1 (Cat #GTX124280) antibodies were from Genetex. dsRNA J2 antibody (Cat #10010200) was procured from Scicons. Phospho PINK1 (Cat #PA5-105356), PINK1 (Cat #PA5-86941), CoV-2 nucleocapsid (Cat #MA5-36272), GAPDH (Cat #MA5-15738), β-Tubulin (Cat #MA5-16308), ACE2 (Cat #MA5-32307) were procured from Thermo Fisher Scientific. Goat Anti-rabbit HRP conjugated (Cat #115-035-146), Alexa Flour 488 conjugated (Cat #115-545-146), Alexa Four 647 conjugated (Cat #115-605-146) and Goat anti-mouse HRP conjugated (Cat #115-035-003), Alexa Flour 488 conjugated (Cat #115-545-003), Alexa Flour 647 conjugated (Cat #115-605-003) were purchased from Jakson ImmunoResearch.

Inhibitors and reagents

Human IFNα 2a (Cat #11100) was purchased from PBL assay science. Poly (I:C) (Cat #P1530), BAY-11-7082 (NF-κB inhibitor, Cat #196870), Baricitinib (JAK-STAT inhibitor, Cat #SBR00076) and Carbonyl Cyanide m-Chlorophenylhydrazone (CCCP, Cat #C2759) and 1-methyl-4-phenyl-1,2,3,6-tetrahydropyridine (MPTP, Cat #M0896) was from Sigma-Aldrich. Human Type I IFN Neutralizing Antibody Mixture (Cat #39000) was from PBL assay science. Human IFN-lambda was from R & D systems (Cat # 1598-IL) Human IFN alpha ELISA Kit (Cat #BMS216), Mitotracker Green dye (Cat #M46750) and JC-1 dye (Cat #T3168) was from Invitrogen. Mitotracker Red (CMX-ROS) dye (Cat #9082) was from Cell Signaling Technologies (CST).

Plasmids and cloning

Mammalian expression vector, pcDNA4/TO was from Invitrogen. Mammalian expression vector pUNO, RIG-I, MDA-5, HA-TBK1, HA-MAVS were from Invivogen. HA-IRF3, Phosphomimetic IRF3 (S396E) and HA-ΔCARD-MAVS were cloned as reported previously (*82*). Mouse MAVS was amplified using cDNA of MEFs and cloned into pcDNA4/TO. Mitophagic flux was assessed by using a p-mito-mRFP-EGFP plasmid (Plasmid pAT016) (*83*).

Generation of MAVS and IFNAR1 Double KO MEFs

All mice were bred and maintained under specific pathogen-free conditions at the CCMB Animal Facility. Double knockout mice for MAVS and IFNAR1 were

generated using MAVS KO males (B6129SF2/J, #008634, Jackson Laboratory) and IFNAR1 KO females (C57BL/6J, #028288). Appropriate animal ethical clearances were obtained from the Institutional Animal Ethics Committee of CCMB and their guidelines were strictly followed. First-generation (G1) heterozygous offspring (MAVS +/-; IFNAR1 +/-) were genotyped and interbred to produce G2 mice, including double homozygotes (MAVS -/-; IFNAR1 -/-). Genomic DNA was prepared from their tail samples (1–2 mm). Were genotyped by PCR using gene-specific primers targeting wild-type and mutant alleles. Amplicons were analyzed via agarose gel electrophoresis. MAVS KO yielded a 350 bp band, IFNAR1 KO a ~450 bp band, and heterozygotes showed both bands. Thermal cycling conditions were optimized separately for each gene.

Cell culture

Caco2 and Calu-3 cells were obtained from ATCC, while Huh7 cells were generously provided by Ralf Bartenschlager (*84*). A549 WT and MAVS KO cells were from Invivogen. MEFs were isolated from WT, MAVS KO, IFNAR1 KO, and MAVS:IFNAR1 DKO mice following the established protocol (*85*). All cells, except for Caco2 (20% FBS), were maintained in DMEM (Gibco) supplemented with 10% FBS (Gibco), 1× penicillin-streptomycin cocktail (Gibco), and 1× non-essential amino acids (Gibco) at 37°C with 5% CO2. Cells were routinely passaged at 70–80% confluency, and mycoplasma contamination was periodically monitored.

Generation of MAVS KO Huh7

MAVS KO Huh7 cells were generated using the CRISPR-Cas9 system. Single-guide RNAs (sgRNAs) targeting exon 6 of the MAVS gene inserted into the PX459 vector containing WT Cas9 (Addgene, Cat #62988). Huh7 cells were transfected with the sgRNA-containing PX459 plasmids using Lipofectamine 3000. Following transfection, puromycin selection was used to enrich transfected cells. Knockout validation was performed by immunoblotting to confirm the loss of MAVS protein. Successfully edited clones were expanded and verified as MAVS knockout Huh7 cells. The following sgRNA primers were used:

Exon Details	sgRNA targeting Exon 6 of MAVS
Target sequence	CGATGCCCGCTGGAGGTCAGAGGGCAAA
Complementary sequence	CACCGCTACGGGCGACCTCCAGTCTCCC

JEV, DENV and CoV-2 isolates

The five variant isolates of CoV-2 used in this study were isolated at the Centre for Cellular and Molecular Biology in the biosafety level 3 facility (*37*). The viruses were propagated in Vero (CCL-81) cells grown in serum free DMEM. JEV and DENV were propagated as previously described (*82*).

Virus Infection and quantification

Cells were infected at 1 MOI for 3 hrs in serum-free conditions after which the media was replaced with complete media and further incubated until the time of harvesting as per experiment requirement. During harvesting, the cells were first trypsinized and collected separately for protein and RNA study. Titration for CoV-2, JEV and DENV were done as described (*37, 82*). For Overexpression studies, cells were seeded to reach 50 to 60% confluency. Transfection mix containing Opti-MEM, Lipofectamine 3000, along with plasmid of interest was prepared according to the manufacturer's protocol, added to cells, and incubated for 6 h. Later, the transfection mix was replaced with cDMEM and further incubated for 18 h. 24 hours post transfection, cells were infected with virus for 3 h and further incubated in fresh cDMEM until they were harvested for analyses. Similar approach was used for Poly(I·C) transfections.

For IFN-α and IFNλ-1 treatment, cells were serum-starved at 80 to 85% confluency in serum-free DMEM (SFD) for 3 h. Later, SFD was replaced with fresh SFD containing 1000 U/mL IFN-α or IFNλ-1 for 1 h. Following this, the cells were infected for 3 h, and incubated further with fresh cDMEM containing either phosphate-buffered saline (PBS; vehicle) or 1,000 U/mL of IFN-α or IFNλ-1, and incubated for

the subsequent 21 h. Cells and culture supernatants were harvested at 24 hpi and used for further analysis.

For Baricitinib and BAY-11-7082 treatments, Cells were treated with the inhibitors 3 hpi and incubated for the subsequent 21 h. For CCCP and MPTP treatments, cell culture media was removed and cells were supplemented with CCCP containing cDMEM 2 hours and 6 hours before harvesting, respectively. Cells and Cell culture supernatants were harvested and used for further analysis.

Real-Time quantitative RT-PCR (qRT-PCR)

Cellular RNA samples were prepared using an MN NucleoSpin RNA kit (TaKaRa, Cat #740902). Equal quantities of RNA were reverse transcribed using Primescript 1st strand cDNA synthesis kit (TaKaRa, Cat #6110) following the manufacturer's protocol. 50 ng of cDNA was used for quantification using TB Green Premix (TaKaRa, Cat #RR820) on a LightCycler 480 instrument (Roche). Transcripts of the host origin were normalized against GAPDH. qRT-PCR to quantify CoV-2 RNA was performed on a Roche LightCycler 480 using an nCOV-19 reverse transcription-PCR (RT-PCR) detection kit from Q-Line Molecular (Cat #COVIDM96PS). Relative fold changes between the experimental and control samples (2–ΔΔCT) were calculated and represented in the graphs. Primer sequences for *IFNB1* and *DENV* are reported earlier (*82*). The following primers were used for qRT-PCR of *IFNL1*:

Forward Primer	Reverse Primer
GGTGACTTTGGTGCTAGGCT	TGAGTGACTCTTCCAAGGCG

Immunoblotting

Cell pellets were lysed in 1 × Nonidet P-40 lysis buffer (1% Nonidet P-40, 50 mM Tris-HCl, 150 mM NaCl (pH 7.5), EGTA, 1 mM sodium orthovanadate, 10 mM sodium pyrophosphate, 100 mM NaF, and 1 mM PMSF), incubated on ice for 20 minutes with intermittent vortexing and centrifuged at 13,000 rpm for 15 minutes at 4°C. The supernatants containing the proteins were collected and quantified using BCA reagents (Pierce, Cat #23225). Lysates were mixed with 6× denaturing dye and

the proteins were resolved using SDS-PAGE and transferred to PVDF membranes. The membranes were blocked in 5% BSA dissolved in 1× TBST before the addition of primary antibodies. Primary antibodies against the proteins of interest were diluted in the blocking buffer, added to the membrane, and incubated overnight at 4°C. Later, the membranes were washed in 1× TBST, secondary antibodies conjugated with HRP were added and the blots were developed on a Bio-Rad Chemidoc MP system using Clarity Western ECL substrate (Biorad, Cat #1705061) and Clarity Max Western ECL substrate (Biorad, Cat #1705062) chemiluminescent substrate kits. Relative fold changes in protein expression between the experimental and control samples were determined and depicted in the graphs.

SDD-AGE

To assess MAVS aggregation, semi-denaturing detergent agarose gel electrophoresis (SDD-AGE) was performed following established protocols (*48, 86*). Briefly, cells were lysed in the presence of protease inhibitors, and lysates were prepared using a dounce homogenizer. Samples were mixed with loading buffer and resolved on 1.5% agarose gels in TAE buffer supplemented with 0.1% SDS under semi-denaturing conditions. Electrophoresis was conducted at 100 V for 45 minutes at 4°C. Proteins were transferred to nitrocellulose membranes via capillary transfer and subsequently detected by immunoblotting with specific antibodies.

Seahorse Mito stress assay

Mitochondrial oxygen consumption was assessed using a Seahorse XFe 24 Analyzer. In summary, 50,000 cells per well were plated in XFe 24 plates, washed twice with DPBS, and incubated for 1 hour at 37 °C in a CO_2 -free incubator with XFe DMEM assay medium containing 10 mM glucose, 2 mM L-glutamine, and 1 mM sodium pyruvate. Oligomycin (3.5 μM), FCCP (3 μM), and a combination of antimycin A (1.5 μM) with rotenone (1.5 μM) were introduced through reagent ports A, B, and C, respectively. Measurements were taken for basal oxygen consumption rate (OCR), ATP-linked OCR, and proton leak, with all values normalized to total protein content determined using the Bradford assay.

For overexpression studies, cells were transfected with the appropriate plasmids in 6-well plates for 24 hours, followed by trypsinization and reseeding at a density of

50,000 cells per well in XFe 24 plates. After reseeding, the same Seahorse assay procedure was carried out as previously described.

Preparation and NMR Analysis of Metabolites from Cell Pellets

Cells incubated with medium containing [1,6-^{13}C] glucose for 45 minutes were harvested and stored at -80°C for further analysis. Metabolites were then extracted from harvested cells using an ethanol-based extraction protocol (*87*). In brief, cells pellet was homogenized in methanol-HCl (0.1N) in (2:1 vol/wt) using a battery-operated tissue homogenizer. [2-^{13}C] Glycine (50 µL, 2 mmol/L) was added as an internal reference, followed by homogenization with ethanol (90%)-phosphate buffer (6:1 vol/vol). The homogenate was centrifuged (20,000 g, 45 min, 4°C), and the supernatant pH-adjusted, and freeze-dried. The lyophilized powder was dissolved in phosphate buffer (25 mmol/L, pH 7.0, 80% D_2O) containing sodium trimethylsilyl propionate (0.25 mmol/L) for NMR measurements. Total and ^{13}C-labeled concentrations of metabolites were measured in ^{1}H-[^{13}C]-NMR spectrum at 600 MHz NMR spectrometer (*88*). The ^{13}C-edited spectrum was obtained through spin-echo acquisition with and without a ^{13}C inversion pulse. Metabolite levels were quantified relative to [2-^{13}C] glycine, and ^{13}C enrichment was corrected for natural abundance (subtracting 1.1%). The rate of glucose consumption (MR Glc) as calculated from the ^{13}C labelled trapped into different metabolites (*89*). The rate of ATP synthesis was calculated as described previously using an approximation of 2.5 and 1.5 ATP yield for each molecule of NADH and FADH, respectively:

ATP syn = (2 NADH + 2 ATP) x Lac Syn + (10 NADH + 2 $FADH_2$ + 4 ATP) x MR Glc (Lac Syn is rate of lactate synthesis).

Microscopy experiments

JC-1 Staining

50,000 cells were seeded in 6-well plates and allowed to adhere overnight. Cells were subjected to experimental conditions (virus infection, treatments, overexpression, or phenotype comparison), washed twice with SFD, and stained with 10 µM JC-1 dye in SFD for 20–30 minutes at 37°C in the dark. After staining, cells were washed twice with SFD, replenished with fresh SFD, and imaged using a

Zeiss Axio Observer 3 microscope with FITC and mCherry filters to visualize green JC-1 monomers and red aggregates.

Mitotracker Red/Green staining

50,000 cells were seeded on coverslips in 6-well plates, subjected to experimental conditions, washed twice with SFD, and incubated with 100 nM Mitotracker Red or Mitotracker Green in SFD for 20–30 minutes at 37°C in the dark. After staining, cells were washed twice with SFD, fixed with 4% formaldehyde for 30 minutes in case of Mitotracker Red, washed with PBS, and stored at 4°C before immunostaining. For mitotracker Green, cells were washed twice with SFD, replenished with fresh SFD, and imaged with a Zeiss Axio Observer 3 microscope using FITC filters.

Mito-GFP-RFP Reporter Assay

50,000 cells were seeded on coverslips, transfected with 2 µg of Mito-GFP-RFP reporter plasmid, and subjected to experimental conditions 24 hours post transfection. Cells were washed twice with PBS, fixed with 4% formaldehyde for 30 minutes, washed with PBS, and stored at 4°C before immunostaining.

Immunostaining

Fixed coverslips were washed twice with PBS, permeabilized (0.05% Tween-20, 0.25% Triton X-100 in PBS) for 10 minutes, and washed three times with PBST. Blocking was performed with 1% BSA and glycine in PBST. Coverslips were incubated overnight at 4°C with primary antibodies diluted in 1% BSA in PBST. After washing, fluorophore-conjugated secondary antibodies were added, followed by three washes with PBST. Coverslips were mounted with DAPI-containing anti-fade mountant (Cat #H-1200-10) and analyzed by microscopy.

Imaging and Analysis

Confocal microscopy was performed using an Olympus FV3000 and Leica SP8 microscopes (60× oil immersion objective for Olympus FV3000, 63x oil immersion objective for Leica SP8, 2.5× optical zoom). Super-resolution imaging was conducted using a ZEISS Elyra 7 system with Lattice SIM² (100× objective, variable zoom). Mitochondrial fragmentation, volume analysis of clumped mitochondria (in CoV-2

and JEV-infected cells) were analyzed using Imaris software. Mitotracker Green intensity, JC-1 red/green ratios and co-localization (e.g., GFP-RFP, MAVS-mitochondria) were quantified with ImageJ.

Intersection density and spatial proximity analysis

Confocal images of Huh7 WT and MAVS KO cells were acquired using the Olympus FV3000 system. Post-acquisition, image stacks containing TOM20, TOM70, and Mitotracker Red channels were deconvolved using the DeconvolutionLab2 plugin in ImageJ, applying the Richardson–Lucy algorithm (20 iterations). Following deconvolution, TOM20 and TOM70 channels were merged, thresholded, and intersection masks were generated using ImageJ's Image Calculator function. Intersections were quantified using the Analyse Particles tool. Mitochondrial area was determined from the Mitotracker Red channel, and intersection density was calculated as the number of TOM20–TOM70 intersections per unit mitochondrial area. For spatial proximity analysis, deconvolved TOM20 and TOM70 images were thresholded, and centroid-to-centroid distances were computed using the MorphoLibJ plugin in ImageJ.

Next-generation sequencing

Library preparation was done using the MGIEasy RNA library prep set (MGI) according to the manufacturer's instructions. In brief, 500 ng total RNA was used as starting material from which rRNA was depleted using a Ribo-Zero Plus rRNA depletion kit (Illumina). The rRNA-depleted samples were fragmented and reverse transcribed, and the second strands were synthesized. DNA was then purified using DNA clean beads provided in the kit, followed by end repair and A-tailing. Barcoding and adaptor ligation were performed, and the samples were purified. Samples were amplified using adaptor-specific primers and quantified using a Qubit dsDNA high-sensitivity kit (Thermo Scientific). Sample fragment size was determined using a 4200 Tape Station (Agilent). The samples were denatured, and single-stranded circular DNA strands were generated. Further, rolling cycle amplification was performed to generate DNA nanoballs. The samples were subsequently loaded onto the flow cells (FCL) and paired end RNA sequencing was performed at MGI 2000 (MGI) platform for read length of 100 bases.

Data processing and analysis

Raw sequencing reads were processed using Cutadapt (*90*) to remove MGI adapters and low-quality sequences. Reads with a quality score below 20 and a length shorter than 36 bp were discarded. The remaining high-quality reads were mapped to the human reference genome (GRCh38) using HISAT2 with default parameters (*91*). Uniquely aligned reads were quantified using the featureCounts function from the Subread package (*92*), based on a GTF annotation file downloaded from Ensembl (*93*), which contained read count data for 60,683 genes. Genes with fewer than 10 total read counts across all samples were excluded, resulting in a final dataset of 36,743 genes for further analysis. Differential gene expression analysis was performed using DESeq2 (*94*), with genes considered differentially expressed if they had a P-value < 0.05 and an absolute log2 fold change > 0.58.

Functional enrichment analysis

Functional enrichment analysis was conducted using clusterProfiler (*95*) to identify enriched Gene Ontology (GO) terms. To refine the results, similar enriched terms were merged using the simplify function of clusterProfiler, with a similarity cutoff of 0.5. The p-value was utilized as a criterion for selecting representative terms, while the min method was applied for feature selection. The Wang method was employed to measure similarity. Finally, the top five enriched GO terms for the genes were visualized.

Statistical analysis

For each experiment, at least three independent replicates (until specified) were used to calculate mean ± SEM and plotted graphically wherever indicated. Statistical significance was measured using a two-tailed, unpaired Student t-test, and the resultant p values were represented as *, **, *** indicating p values ≤ 0.05, 0.01, and 0.001, respectively.

Biosafety statement

All infection protocols in this study were approved by the Institute Biosafety Committee of CSIR-CCMB.

Ethical Statement

All animal protocols in this study were approved by the Institute Animal Ethics Committee of CSIR-CCMB.

Data availability

All data pertaining to this manuscript are included within the manuscript. The RNA sequencing (RNA-seq) data have been submitted to the Gene Expression Omnibus (GEO) database and are available under the accession number GSE293066.

Funding

This work was supported by funding from the Council of Scientific and Industrial Research, Government of India (6/1/FIRST/2020-RPPBDD-TMD-SeMI), and from Indian Council of Medical Research (ICMR), Government of India (EMDR/CARE/12/2023-0000176) to K.H.H. V.S. received fellowship from the Department of Biotechnology (DBT), Government of India. P.S.P received fellowship from the Department of Science and Technology (DST-INSPIRE), P.P.S and D.T received fellowships from Council of Scientific and Industrial Research (CSIR), Government of India, respectively.

ACKNOWLEDGEMENTS

We thank Dr. Shasi Vardhan Kalivendi, Dr. Chitrakshi Pant and Abhijit Mohapatra for assistance with Seahorse Experiments. We also thank Dr. Nitesh Kumar Singh for help with the preliminary RNA-seq datasets. We thank Dr. Sudhanshu Vrati for sharing the mito-GFP-RFP plasmid. Special appreciation to Mohan Singh Moodu and Amit Kumar for their assistance with experimental logistics. We also thank Dr. C. Subbulakshmi, Dr. Venkata Mahesh Nitla and Suman Bandari for their help with confocal imaging and analysis, and N Sai Ram, Dr. M Jerald Mahesh Kumar and B Jyothi Lakshmi from CCMB Animal Facility.

AUTHOR CONTRIBUTIONS

V.S and K.H.H conceived and designed this study. V.S, P.S.P, and K.H.H designed the experiments. V.S, P.S.P, K.S.N, and A.R.P performed the overexpression and KO studies. A.R.P and D.T. performed the IFN treatment studies. V.S and D.B

generated MAVS KO Huh7 cells. P.P.S generated and verified the MAVS/IFNAR1 DKO mice. V.S, P.S.P, P.P.S, and D.T isolated MEFs for this study. V.S analysed the next-generation sequencing data with assistance from D.T. A.B.P, and K.S.V performed NMR experiments. S.C provided IFNAR1 KO mice. K.H.H and V.S wrote the manuscript with inputs from S.P, D.T, and P.P.S.

REFERENCES

1. M. Yoneyama *et al.*, The RNA helicase RIG-I has an essential function in double-stranded RNA-induced innate antiviral responses. *Nature Immunology* **5**, 730-737 (2004).
2. J. Andrejeva *et al.*, The V proteins of paramyxoviruses bind the IFN-inducible RNA helicase, mda-5, and inhibit its activation of the IFN-β promoter. *Proceedings of the National Academy of Sciences* **101**, 17264-17269 (2004).
3. R. B. Seth, L. Sun, C.-K. Ea, Z. J. Chen, Identification and Characterization of MAVS, a Mitochondrial Antiviral Signaling Protein that Activates NF-κB and IRF3. *Cell* **122**, 669-682 (2005).
4. E. Dixit *et al.*, Peroxisomes Are Signaling Platforms for Antiviral Innate Immunity. *Cell* **141**, 668-681 (2010).
5. M. Sato *et al.*, Distinct and Essential Roles of Transcription Factors IRF-3 and IRF-7 in Response to Viruses for IFN-α/β Gene Induction. *Immunity* **13**, 539-548 (2000).
6. Z. He *et al.*, Dengue Virus Subverts Host Innate Immunity by Targeting Adaptor Protein MAVS. *Journal of Virology* **90**, 7219-7230 (2016).
7. X.-D. Li, L. Sun, R. B. Seth, G. Pineda, Z. J. Chen, Hepatitis C virus protease NS3/4A cleaves mitochondrial antiviral signaling protein off the mitochondria to evade innate immunity. *Proceedings of the National Academy of Sciences* **102**, 17717-17722 (2005).
8. C.-S. Shi *et al.*, SARS-Coronavirus Open Reading Frame-9b Suppresses Innate Immunity by Targeting Mitochondria and the MAVS/TRAF3/TRAF6 Signalosome. *The Journal of Immunology* **193**, 3080-3089 (2014).
9. D. Zhou *et al.*, The Japanese Encephalitis Virus NS1′ Protein Inhibits Type I IFN Production by Targeting MAVS. *The Journal of Immunology* **204**, 1287-1298 (2020).
10. W.-H. Shao *et al.*, Prion-like Aggregation of Mitochondrial Antiviral Signaling Protein in Lupus Patients Is Associated With Increased Levels of Type I Interferon. *Arthritis & Rheumatology* **68**, 2697-2707 (2016).
11. W. Sun *et al.*, Antiviral Adaptor MAVS Promotes Murine Lupus With a B Cell Autonomous Role. *Frontiers in Immunology* **Volume 10 - 2019**, (2019).
12. S. M. Horner, H. M. Liu, H. S. Park, J. Briley, M. Gale, Mitochondrial-associated endoplasmic reticulum membranes (MAM) form innate immune synapses and are targeted by hepatitis C virus. *Proceedings of the National Academy of Sciences* **108**, 14590-14595 (2011).
13. J. L. Jacobs, J. Zhu, S. N. Sarkar, C. B. Coyne, Regulation of Mitochondrial Antiviral Signaling (MAVS) Expression and Signaling by the Mitochondria-associated Endoplasmic Reticulum Membrane (MAM) Protein Gp78 *. *Journal of Biological Chemistry* **289**, 1604-1616 (2014).

14. E. I. Elliott, F. S. Sutterwala, Initiation and perpetuation of NLRP3 inflammasome activation and assembly. *Immunological Reviews* **265**, 35-52 (2015).
15. Q. Liu, D. Zhang, D. Hu, X. Zhou, Y. Zhou, The role of mitochondria in NLRP3 inflammasome activation. *Molecular Immunology* **103**, 115-124 (2018).
16. M. Khan, G. H. Syed, S.-J. Kim, A. Siddiqui, Mitochondrial dynamics and viral infections: A close nexus. *Biochimica et Biophysica Acta (BBA) - Molecular Cell Research* **1853**, 2822-2833 (2015).
17. S.-J. Kim *et al.*, Hepatitis C virus triggers mitochondrial fission and attenuates apoptosis to promote viral persistence. *Proceedings of the National Academy of Sciences* **111**, 6413-6418 (2014).
18. C. Castanier, D. Garcin, A. Vazquez, D. Arnoult, Mitochondrial dynamics regulate the RIG-I-like receptor antiviral pathway. *EMBO reports* **11**, 133-138-138 (2010).
19. M. Pourcelot, D. Arnoult, Mitochondrial dynamics and the innate antiviral immune response. *The FEBS Journal* **281**, 3791-3802 (2014).
20. M. Li *et al.*, Integrated Metabolomics and Transcriptomics Analyses Reveal Metabolic Landscape in Neuronal Cells during JEV Infection. *Virologica Sinica* **36**, 1554-1565 (2021).
21. P. Mingo-Casas *et al.*, Glycolytic shift during West Nile virus infection provides new therapeutic opportunities. *Journal of Neuroinflammation* **20**, 217 (2023).
22. D. Passalacqua Karla *et al.*, Glycolysis Is an Intrinsic Factor for Optimal Replication of a Norovirus. *mBio* **10**, 10.1128/mbio.02175-02118 (2019).
23. A. C. Codo *et al.*, Elevated Glucose Levels Favor SARS-CoV-2 Infection and Monocyte Response through a HIF-1α/Glycolysis-Dependent Axis. *Cell Metabolism* **32**, 437-446.e435 (2020).
24. P. Goyal, M. S. Rajala, Reprogramming of glucose metabolism in virus infected cells. *Molecular and Cellular Biochemistry* **478**, 2409-2418 (2023).
25. J. Kleinehr *et al.*, Glycolytic interference blocks influenza A virus propagation by impairing viral polymerase-driven synthesis of genomic vRNA. *PLOS Pathogens* **19**, e1010986 (2023).
26. A. N. Bhatt *et al.*, Glycolytic inhibitor 2-deoxy-d-glucose attenuates SARS-CoV-2 multiplication in host cells and weakens the infective potential of progeny virions. *Life Sciences* **295**, 120411 (2022).
27. S. Anderson *et al.*, Sequence and organization of the human mitochondrial genome. *Nature* **290**, 457-465 (1981).
28. S. Franco-Iborra *et al.*, Defective mitochondrial protein import contributes to complex I-induced mitochondrial dysfunction and neurodegeneration in Parkinson's disease. *Cell Death & Disease* **9**, 1122 (2018).
29. Y. Fukasawa, T. Oda, K. Tomii, K. Imai, Origin and Evolutionary Alteration of the Mitochondrial Import System in Eukaryotic Lineages. *Molecular Biology and Evolution* **34**, 1574-1586 (2017).
30. R. S. Freitas, T. F. Crum, K. Parvatiyar, SARS-CoV-2 Spike Antagonizes Innate Antiviral Immunity by Targeting Interferon Regulatory Factor 3. *Frontiers in Cellular and Infection Microbiology* **Volume 11 - 2021**, (2022).
31. S. J. Oh, O. S. Shin, SARS-CoV-2 Nucleocapsid Protein Targets RIG-I-Like Receptor Pathways to Inhibit the Induction of Interferon Response. *Cells*. 2021 (10.3390/cells10030530).
32. D. Zhang *et al.*, SARS-CoV-2 Nsp15 suppresses type I interferon production by inhibiting IRF3 phosphorylation and nuclear translocation. *iScience* **26**, (2023).

33. K. Feng *et al.*, SARS-CoV-2 NSP13 interacts with host IRF3, blocking antiviral immune responses. *Journal of Medical Virology* **95**, e28881 (2023).
34. J. Deng *et al.*, SARS-CoV-2 NSP7 inhibits type I and III IFN production by targeting the RIG-I/MDA5, TRIF, and STING signaling pathways. *Journal of Medical Virology* **95**, e28561 (2023).
35. Y. Zheng *et al.*, SARS-CoV-2 NSP5 and N protein counteract the RIG-I signaling pathway by suppressing the formation of stress granules. *Signal Transduction and Targeted Therapy* **7**, 22 (2022).
36. L. Sui *et al.*, SARS-CoV-2 Membrane Protein Inhibits Type I Interferon Production Through Ubiquitin-Mediated Degradation of TBK1. *Frontiers in Immunology* **Volume 12 - 2021**, (2021).
37. D. Tandel *et al.*, SARS-CoV-2 Variant Delta Potently Suppresses Innate Immune Response and Evades Interferon-Activated Antiviral Responses in Human Colon Epithelial Cells. *Microbiology Spectrum* **10**, e01604-01622 (2022).
38. Z. Yao, L. Zhang, Y. Duan, X. Tang, J. Lu, Molecular insights into the adaptive evolution of SARS-CoV-2 spike protein. *Journal of Infection* **88**, (2024).
39. C. Shang *et al.*, SARS-CoV-2 Causes Mitochondrial Dysfunction and Mitophagy Impairment. *Frontiers in Microbiology* **Volume 12 - 2021**, (2022).
40. B. Singh *et al.*, Defective Mitochondrial Quality Control during Dengue Infection Contributes to Disease Pathogenesis. *Journal of Virology* **96**, e00828-00822 (2022).
41. D. K. Beyer, A. Forero, Mechanisms of Antiviral Immune Evasion of SARS-CoV-2. *Journal of Molecular Biology* **434**, 167265 (2022).
42. J. M. Minkoff, B. tenOever, Innate immune evasion strategies of SARS-CoV-2. *Nature Reviews Microbiology* **21**, 178-194 (2023).
43. J. K. Sprokholt *et al.*, RIG-I-like receptor activation by dengue virus drives follicular T helper cell formation and antibody production. *PLOS Pathogens* **13**, e1006738 (2017).
44. H. Kato *et al.*, Differential roles of MDA5 and RIG-I helicases in the recognition of RNA viruses. *Nature* **441**, 101-105 (2006).
45. Y. Hanada *et al.*, MAVS is energized by Mff which senses mitochondrial metabolism via AMPK for acute antiviral immunity. *Nature Communications* **11**, 5711 (2020).
46. H. Chu *et al.*, Comparative tropism, replication kinetics, and cell damage profiling of SARS-CoV-2 and SARS-CoV with implications for clinical manifestations, transmissibility, and laboratory studies of COVID-19: an observational study. *The Lancet Microbe* **1**, e14-e23 (2020).
47. X. Lei *et al.*, Activation and evasion of type I interferon responses by SARS-CoV-2. *Nature Communications* **11**, 3810 (2020).
48. F. Hou *et al.*, MAVS Forms Functional Prion-like Aggregates to Activate and Propagate Antiviral Innate Immune Response. *Cell* **146**, 448-461 (2011).
49. C. S. Bartolomeo *et al.*, SARS-CoV-2 infection and replication kinetics in different human cell types: The role of autophagy, cellular metabolism and ACE2 expression. *Life Sciences* **308**, 120930 (2022).
50. F. Le Chevalier *et al.*, Mice humanized for MHC and hACE2 with high permissiveness to SARS-CoV-2 omicron replication. *Microbes and Infection* **25**, 105142 (2023).

51. Y.-C. Chen *et al.*, TOMM40 Genetic Variants Cause Neuroinflammation in Alzheimer's Disease. *International Journal of Molecular Sciences*. 2023 (10.3390/ijms24044085).
52. Y. Ruan *et al.*, CHCHD2 and CHCHD10 regulate mitochondrial dynamics and integrated stress response. *Cell Death & Disease* **13**, 156 (2022).
53. F. Ye *et al.*, CypD deficiency confers neuroprotection against mitochondrial abnormality caused by lead in SH-SY5Y cell. *Toxicology Letters* **323**, 25-34 (2020).
54. C. Carlantoni *et al.*, The phosphodiesterase 2A controls lymphatic junctional maturation via cGMP-dependent notch signaling. *Developmental Cell* **59**, 308-325.e311 (2024).
55. M. Zhang, R. Xiang, C. Glorieux, P. Huang, PLA2G2A Phospholipase Promotes Fatty Acid Synthesis and Energy Metabolism in Pancreatic Cancer Cells with K-ras Mutation. *International Journal of Molecular Sciences*. 2022 (10.3390/ijms231911721).
56. K. H. Ebrahimi *et al.*, Viperin, through its radical-SAM activity, depletes cellular nucleotide pools and interferes with mitochondrial metabolism to inhibit viral replication. *FEBS Letters* **594**, 1624-1630 (2020).
57. M. Zhao *et al.*, Loss of function of CMPK2 causes mitochondria deficiency and brain calcification. *Cell Discovery* **8**, 128 (2022).
58. A. Agarwal *et al.*, Japanese Encephalitis Virus NS4A Protein Interacts with PTEN-Induced Kinase 1 (PINK1) and Promotes Mitophagy in Infected Cells. *Microbiology Spectrum* **10**, e00830-00822 (2022).
59. L. Chatel-Chaix *et al.*, Dengue Virus Perturbs Mitochondrial Morphodynamics to Dampen Innate Immune Responses. *Cell Host & Microbe* **20**, 342-356 (2016).
60. X.-Y. Liu, B. Wei, H.-X. Shi, Y.-F. Shan, C. Wang, Tom70 mediates activation of interferon regulatory factor 3 on mitochondria. *Cell Research* **20**, 994-1011 (2010).
61. P. Rai, M. B. Fessler, The MAVS and MAV-Nots: PINK1 Clears Prion-like MAVS Aggregates to Extinguish Mitochondrial Inflammatory Signaling. *American Journal of Respiratory Cell and Molecular Biology* **64**, 528-530 (2021).
62. O. G. Raimi *et al.*, Mechanism of human PINK1 activation at the TOM complex in a reconstituted system. *Science Advances* **10**, eadn7191 (2024).
63. P. Silwal, J. K. Kim, Y. J. Kim, E.-K. Jo, Mitochondrial Reactive Oxygen Species: Double-Edged Weapon in Host Defense and Pathological Inflammation During Infection. *Frontiers in Immunology* **Volume 11 - 2020**, (2020).
64. K. Onoguchi *et al.*, Virus-Infection or 5′ppp-RNA Activates Antiviral Signal through Redistribution of IPS-1 Mediated by MFN1. *PLOS Pathogens* **6**, e1001012 (2010).
65. S. Chen *et al.*, TBK1-Mediated DRP1 Targeting Confers Nucleic Acid Sensing to Reprogram Mitochondrial Dynamics and Physiology. *Molecular Cell* **80**, 810-827.e817 (2020).
66. J. S. Lee *et al.*, Pressure to evade cell-autonomous innate sensing reveals interplay between mitophagy, IFN signaling, and SARS-CoV-2 evolution. *Cell Reports* **44**, 115115 (2025).
67. K. Yasukawa *et al.*, Mitofusin 2 Inhibits Mitochondrial Antiviral Signaling. *Science Signaling* **2**, ra47-ra47 (2009).

68. T. Koshiba, K. Yasukawa, Y. Yanagi, S.-i. Kawabata, Mitochondrial Membrane Potential Is Required for MAVS-Mediated Antiviral Signaling. *Science Signaling* **4**, ra7-ra7 (2011).
69. H. Wang *et al.*, MAVS Positively Regulates Mitochondrial Integrity and Metabolic Fitness in B Cells. *ImmunoHorizons* **7**, 587-599 (2023).
70. X. Sun *et al.*, MAVS maintains mitochondrial homeostasis via autophagy. *Cell Discovery* **2**, 16024 (2016).
71. L. Wu *et al.*, Noncanonical MAVS signaling restrains dendritic cell–driven antitumor immunity by inhibiting IL-12. *Science Immunology* **8**, eadf4919 (2024).
72. N. Subramanian, K. Natarajan, Menna R. Clatworthy, Z. Wang, Ronald N. Germain, The Adaptor MAVS Promotes NLRP3 Mitochondrial Localization and Inflammasome Activation. *Cell* **153**, 348-361 (2013).
73. M. Khan, G. H. Syed, S.-J. Kim, A. Siddiqui, Hepatitis B Virus-Induced Parkin-Dependent Recruitment of Linear Ubiquitin Assembly Complex (LUBAC) to Mitochondria and Attenuation of Innate Immunity. *PLOS Pathogens* **12**, e1005693 (2016).
74. A. C. Y. Fan *et al.*, Interaction between the Human Mitochondrial Import Receptors Tom20 and Tom70 *in Vitro* Suggests a Chaperone Displacement Mechanism *. *Journal of Biological Chemistry* **286**, 32208-32219 (2011).
75. U. Turakhiya *et al.*, Protein Import by the Mitochondrial Presequence Translocase in the Absence of a Membrane Potential. *Journal of Molecular Biology* **428**, 1041-1052 (2016).
76. M. F. Bauer, C. Sirrenberg, W. Neupert, M. Brunner, Role of Tim23 as Voltage Sensor and Presequence Receptor in Protein Import into Mitochondria. *Cell* **87**, 33-41 (1996).
77. S. Galiani *et al.*, Super-resolution Microscopy Reveals Compartmentalization of Peroxisomal Membrane Proteins *. *Journal of Biological Chemistry* **291**, 16948-16962 (2016).
78. M. A. Carpio *et al.*, BOK controls apoptosis by Ca^{2+} transfer through ER-mitochondrial contact sites. *Cell Reports* **34**, (2021).
79. Y. Lyu, T. Wang, S. Huang, Z. Zhang, Mitochondrial Damage-Associated Molecular Patterns and Metabolism in the Regulation of Innate Immunity. *Journal of Innate Immunity* **15**, 665-679 (2023).
80. N. Kelley, D. Jeltema, Y. Duan, Y. He, The NLRP3 Inflammasome: An Overview of Mechanisms of Activation and Regulation. *International Journal of Molecular Sciences*. 2019 (10.3390/ijms20133328).
81. E. L. Sanchez, M. Lagunoff, Viral activation of cellular metabolism. *Virology* **479-480**, 609-618 (2015).
82. D. Vedagiri *et al.*, Retinoic Acid-Inducible Gene I-Like Receptors Activate Snail To Limit RNA Viral Infections. *Journal of Virology* **95**, 10.1128/jvi.01216-01221 (2021).
83. S.-J. Kim *et al.*, Hepatitis B Virus Disrupts Mitochondrial Dynamics: Induces Fission and Mitophagy to Attenuate Apoptosis. *PLOS Pathogens* **9**, e1003722 (2013).
84. R. Gosert *et al.*, Identification of the Hepatitis C Virus RNA Replication Complex in Huh-7 Cells Harboring Subgenomic Replicons. *Journal of Virology* **77**, 5487-5492 (2003).

85. J. Brugarolas, R. T. Bronson, T. Jacks, p21 Is a Critical CDK2 Regulator Essential for Proliferation Control in Rb-deficient Cells. *Journal of Cell Biology* **141**, 503-514 (1998).
86. S. Alberti, R. Halfmann, O. King, A. Kapila, S. Lindquist, A Systematic Survey Identifies Prions and Illuminates Sequence Features of Prionogenic Proteins. *Cell* **137**, 146-158 (2009).
87. A. B. Patel, D. L. Rothman, G. W. Cline, K. L. Behar, Glutamine is the major precursor for GABA synthesis in rat neocortex in vivo following acute GABA-transaminase inhibition. *Brain Research* **919**, 207-220 (2001).
88. P. Bagga, A. N. Chugani, K. S. Varadarajan, A. B. Patel, In vivo NMR studies of regional cerebral energetics in MPTP model of Parkinson's disease: recovery of cerebral metabolism with acute levodopa treatment. *Journal of Neurochemistry* **127**, 365-377 (2013).
89. P. K. Mishra *et al.*, Impaired neuronal and astroglial metabolic activity in chronic unpredictable mild stress model of depression: Reversal of behavioral and metabolic deficit with lanicemine. *Neurochemistry International* **137**, 104750 (2020).
90. M. Martin, Cutadapt removes adapter sequences from high-throughput sequencing reads. *EMBnet.journal; Vol 17, No 1: Next Generation Sequencing Data AnalysisDO - 10.14806/ej.17.1.200*, (2011).
91. D. Kim, J. M. Paggi, C. Park, C. Bennett, S. L. Salzberg, Graph-based genome alignment and genotyping with HISAT2 and HISAT-genotype. *Nature Biotechnology* **37**, 907-915 (2019).
92. Y. Liao, G. K. Smyth, W. Shi, featureCounts: an efficient general purpose program for assigning sequence reads to genomic features. *Bioinformatics* **30**, 923-930 (2014).
93. K. L. Howe *et al.*, Ensembl 2021. *Nucleic Acids Research* **49**, D884-D891 (2021).
94. M. I. Love, W. Huber, S. Anders, Moderated estimation of fold change and dispersion for RNA-seq data with DESeq2. *Genome Biology* **15**, 550 (2014).
95. T. Wu *et al.*, clusterProfiler 4.0: A universal enrichment tool for interpreting omics data. *The Innovation* **2**, 100141 (2021).

Figure 1

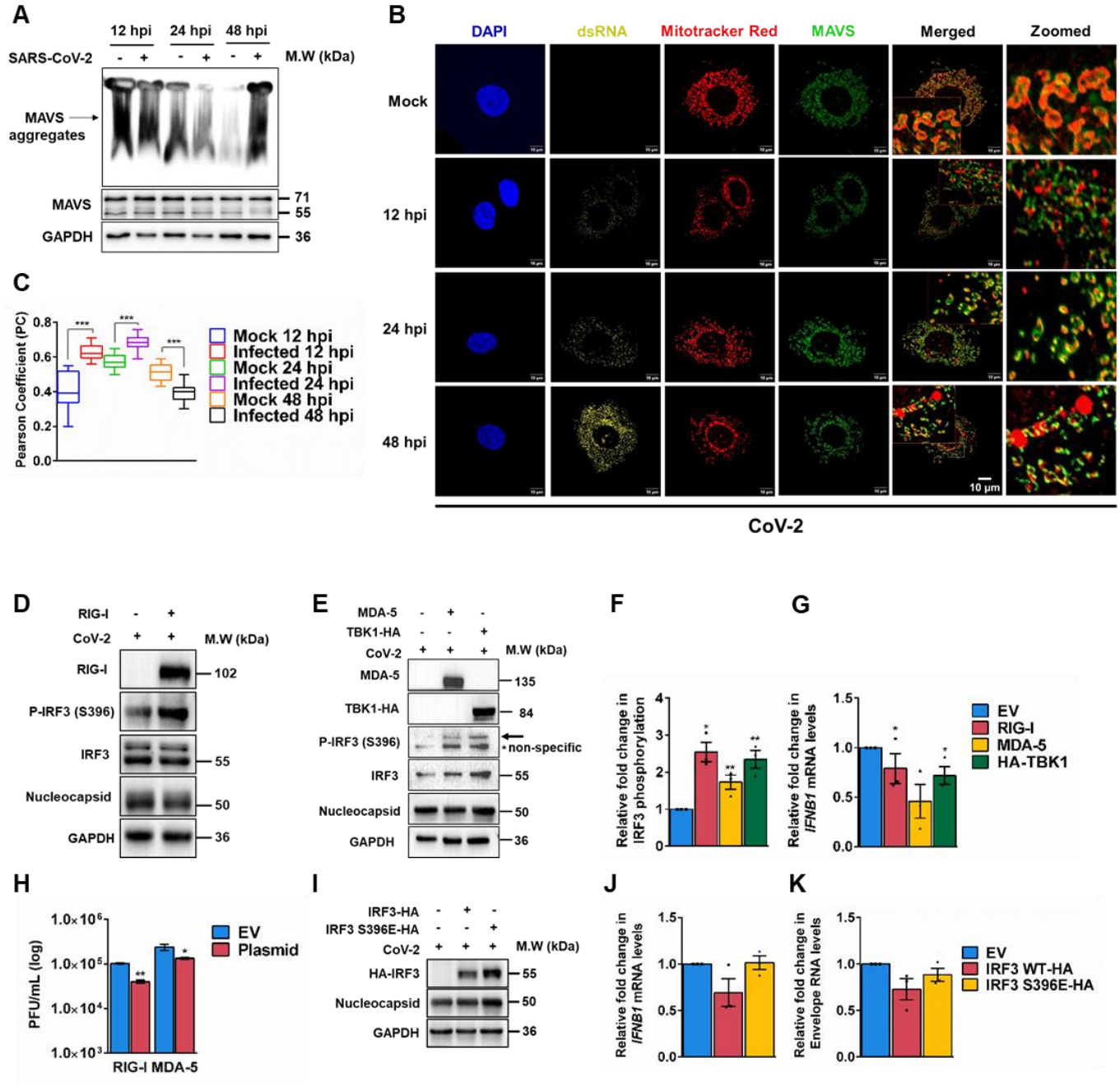
A
12 hpi
24 hpi
48 hpi
SARS-CoV-2
M.W (kDa)
MAVS aggregates
MAVS
GAPDH
71
55
36
B
DAPI
dsRNA
Mitotracker Red
MAVS
Merged
Zoomed
Mock
12 hpi
24 hpi
48 hpi
10 µm
CoV-2
C
Pearson Coefficient (PC)
Mock 12 hpi
Infected 12 hpi
Mock 24 hpi
Infected 24 hpi
Mock 48 hpi
Infected 48 hpi
D
RIG-I
CoV-2
M.W (kDa)
RIG-I
P-IRF3 (S396)
IRF3
Nucleocapsid
GAPDH
102
55
50
36
E
MDA-5
TBK1-HA
CoV-2
M.W (kDa)
MDA-5
TBK1-HA
P-IRF3 (S396)
IRF3
Nucleocapsid
GAPDH
135
84
non-specific
55
50
36
F
Relative fold change in IRF3 phosphorylation
G
Relative fold change in IFNB1 mRNA levels
EV
RIG-I
MDA-5
HA-TBK1
H
PFU/mL (log)
EV
Plasmid
RIG-I
MDA-5
I
IRF3-HA
IRF3 S396E-HA
CoV-2
M.W (kDa)
HA-IRF3
Nucleocapsid
GAPDH
55
50
36
J
Relative fold change in IFNB1 mRNA levels
K
Relative fold change in Envelope RNA levels
EV
IRF3 WT-HA
IRF3 S396E-HA

Figure 2

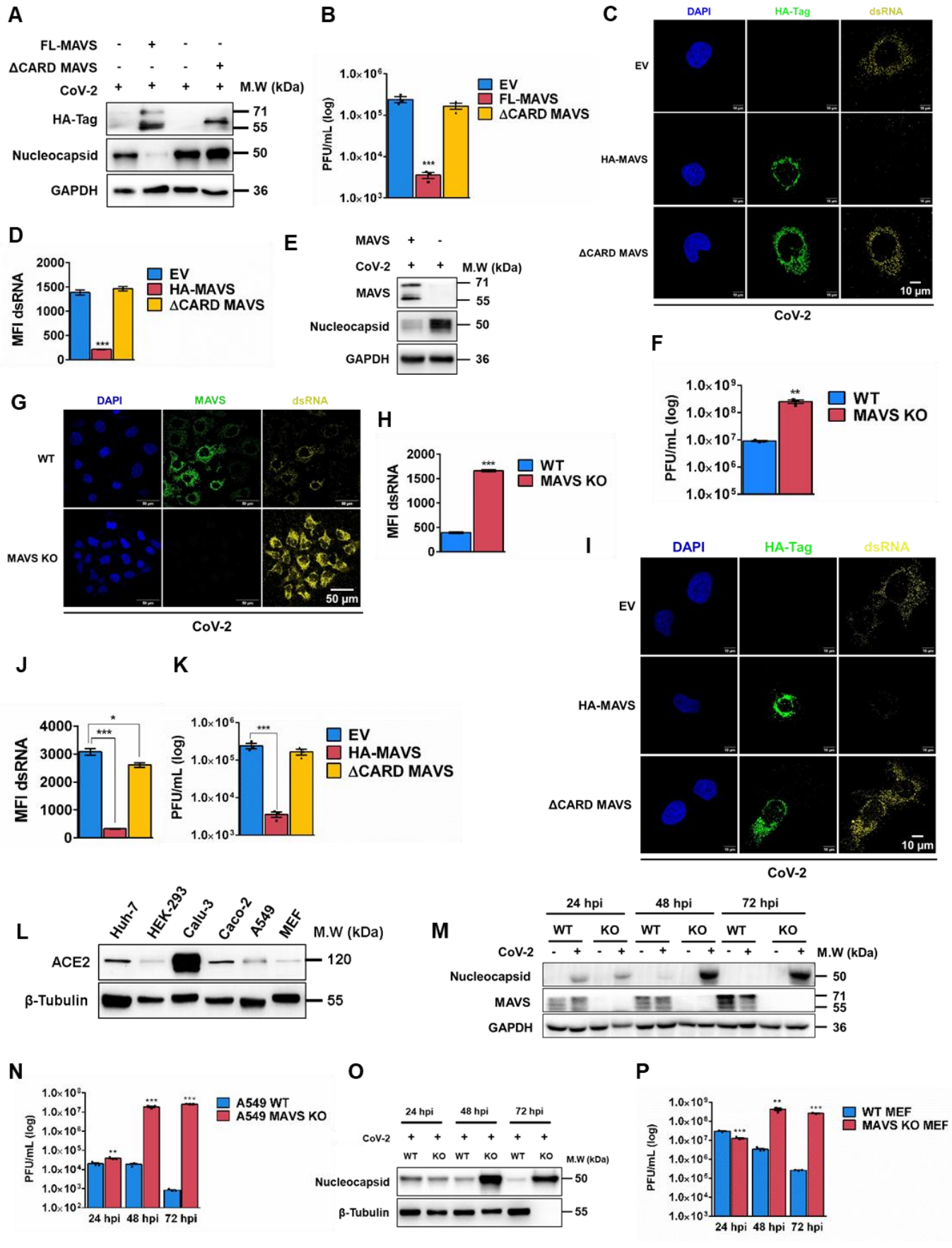
A
FL-MAVS
ΔCARD MAVS
CoV-2
M.W (kDa)
HA-Tag
Nucleocapsid
GAPDH
71
55
50
36
B
PFU/mL (log)
EV
FL-MAVS
ΔCARD MAVS
C
DAPI
HA-Tag
dsRNA
EV
HA-MAVS
ΔCARD MAVS
10 μm
CoV-2
D
MFI dsRNA
EV
HA-MAVS
ΔCARD MAVS
E
MAVS
CoV-2
M.W (kDa)
MAVS
Nucleocapsid
GAPDH
71
55
50
36
F
PFU/mL (log)
WT
MAVS KO
G
DAPI
MAVS
dsRNA
WT
MAVS KO
50 μm
CoV-2
H
MFI dsRNA
WT
MAVS KO
I
DAPI
HA-Tag
dsRNA
EV
HA-MAVS
ΔCARD MAVS
10 μm
CoV-2
J
MFI dsRNA
K
PFU/mL (log)
EV
HA-MAVS
ΔCARD MAVS
L
Huh-7
HEK-293
Calu-3
Caco-2
A549
MEF
M.W (kDa)
ACE2
β-Tubulin
120
55
M
24 hpi
48 hpi
72 hpi
WT
KO
CoV-2
M.W (kDa)
Nucleocapsid
MAVS
GAPDH
50
71
55
36
N
PFU/mL (log)
A549 WT
A549 MAVS KO
24 hpi
48 hpi
72 hpi
O
24 hpi
48 hpi
72 hpi
CoV-2
WT
KO
M.W (kDa)
Nucleocapsid
β-Tubulin
50
55
P
PFU/mL (log)
WT MEF
MAVS KO MEF
24 hpi
48 hpi
72 hpi

Figure 3

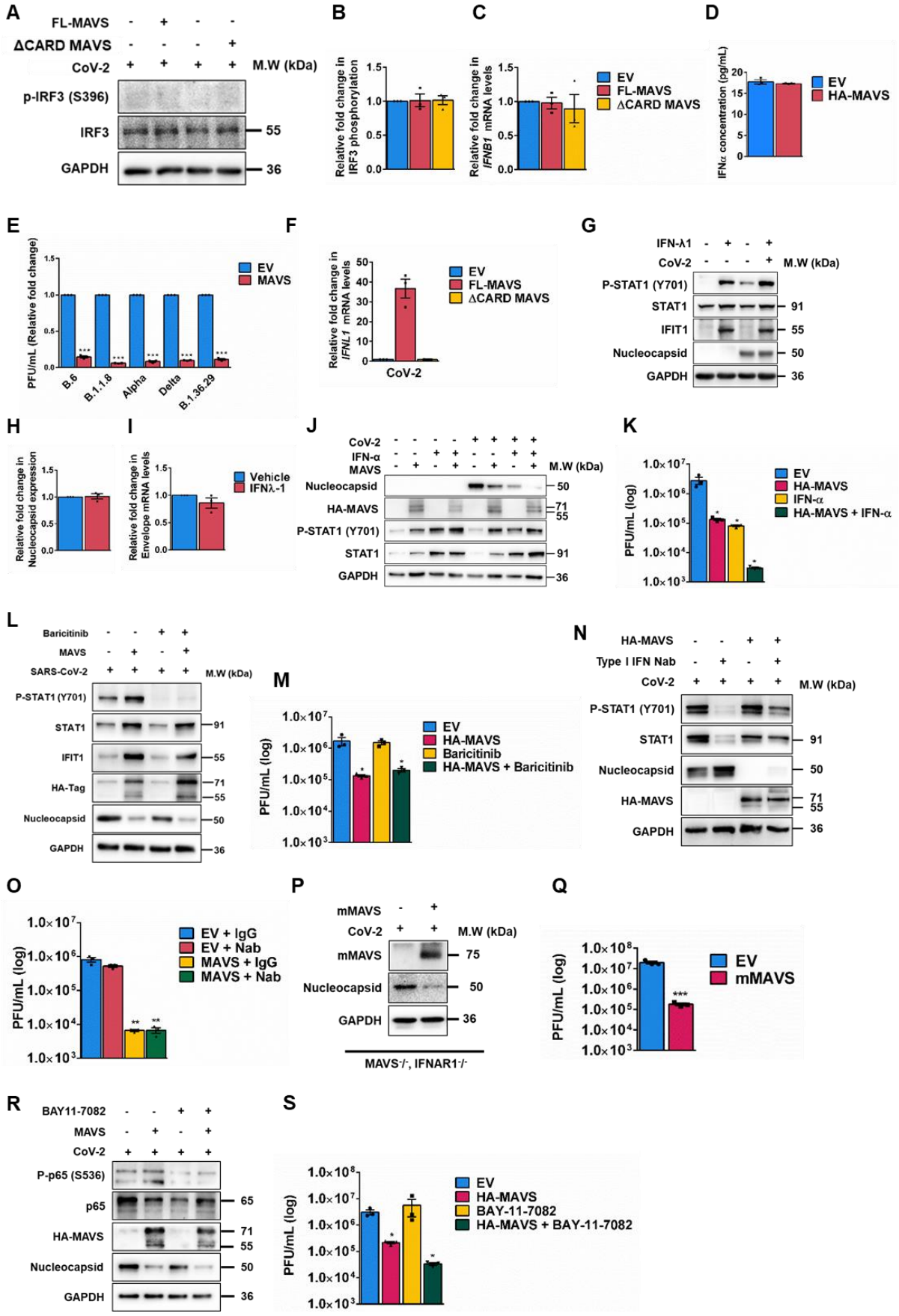
A
FL-MAVS
ΔCARD MAVS
CoV-2
M.W (kDa)
p-IRF3 (S396)
IRF3
GAPDH
55
36
B
Relative fold change in IRF3 phosphorylation
C
Relative fold change in IFNB1 mRNA levels
EV
FL-MAVS
ΔCARD MAVS
D
IFNα concentration (pg/mL)
EV
HA-MAVS
E
PFU/mL (Relative fold change)
EV
MAVS
B.6
B.1.1.8
Alpha
Delta
B.1.36.29
F
Relative fold change in IFNL1 mRNA levels
EV
FL-MAVS
ΔCARD MAVS
CoV-2
G
IFN-λ1
CoV-2
M.W (kDa)
P-STAT1 (Y701)
STAT1
IFIT1
Nucleocapsid
GAPDH
91
55
50
36
H
Relative fold change in Nucleocapsid expression
I
Relative fold change in Envelope mRNA levels
Vehicle
IFNλ-1
J
CoV-2
IFN-α
MAVS
M.W (kDa)
Nucleocapsid
HA-MAVS
P-STAT1 (Y701)
STAT1
GAPDH
50
71
55
91
36
K
PFU/mL (log)
EV
HA-MAVS
IFN-α
HA-MAVS + IFN-α
L
Baricitinib
MAVS
SARS-CoV-2
M.W (kDa)
P-STAT1 (Y701)
STAT1
IFIT1
HA-Tag
Nucleocapsid
GAPDH
91
55
71
55
50
36
M
PFU/mL (log)
EV
HA-MAVS
Baricitinib
HA-MAVS + Baricitinib
N
HA-MAVS
Type I IFN Nab
CoV-2
M.W (kDa)
P-STAT1 (Y701)
STAT1
Nucleocapsid
HA-MAVS
GAPDH
91
50
71
55
36
O
PFU/mL (log)
EV + IgG
EV + Nab
MAVS + IgG
MAVS + Nab
P
mMAVS
CoV-2
M.W (kDa)
mMAVS
Nucleocapsid
GAPDH
75
50
36
MAVS-/-, IFNAR1-/-
Q
PFU/mL (log)
EV
mMAVS
R
BAY11-7082
MAVS
CoV-2
P-p65 (S536)
p65
HA-MAVS
Nucleocapsid
GAPDH
65
71
55
50
36
S
PFU/mL (log)
EV
HA-MAVS
BAY-11-7082
HA-MAVS + BAY-11-7082

Figure 4

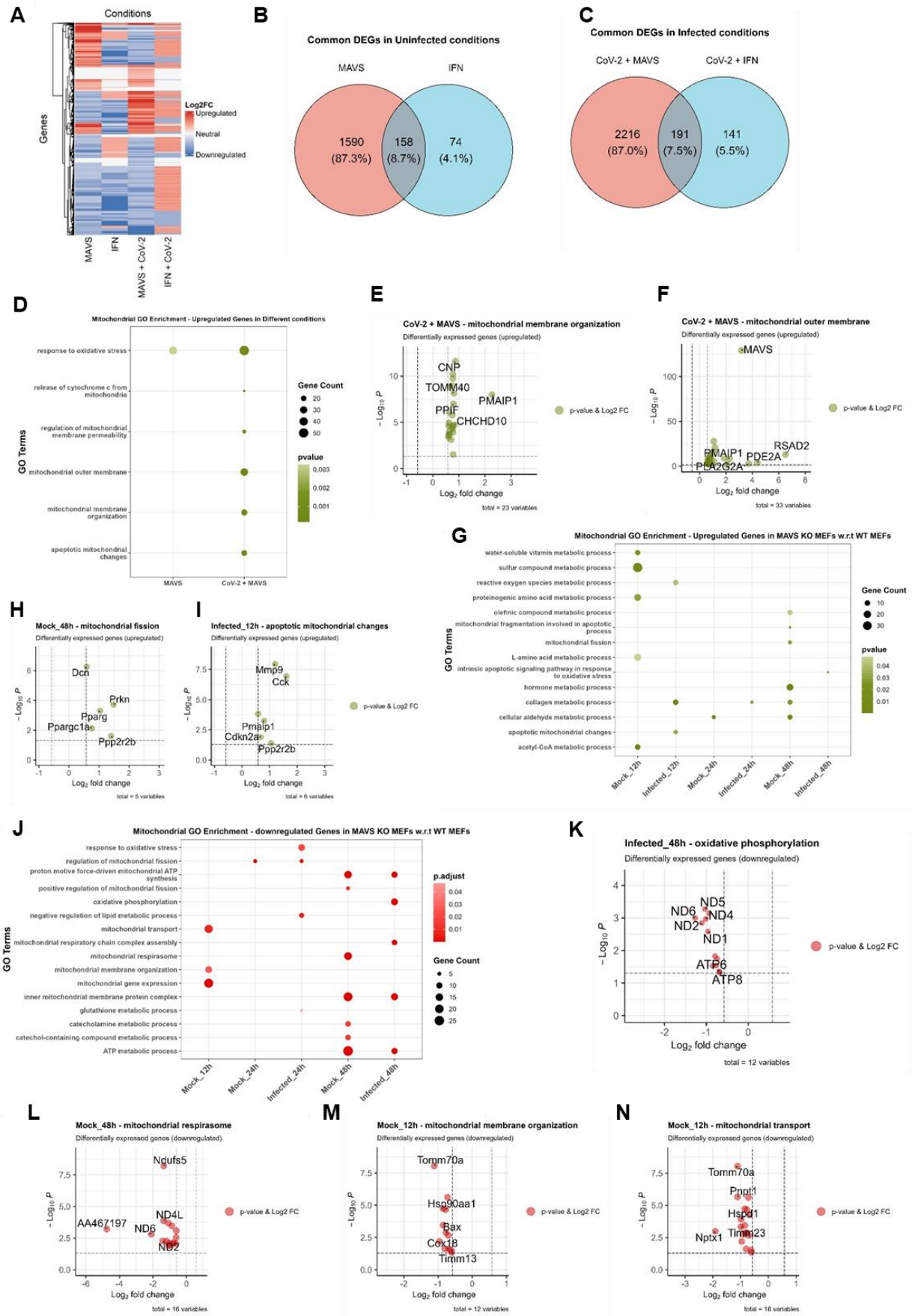
A
Conditions
Genes
Log2FC
Upregulated
Neutral
Downregulated
MAVS
IFN
MAVS + CoV-2
IFN + CoV-2
B
Common DEGs in Uninfected conditions
MAVS
IFN
1590 (87.3%)
158 (8.7%)
74 (4.1%)
C
Common DEGs in Infected conditions
CoV-2 + MAVS
CoV-2 + IFN
2216 (87.0%)
191 (7.5%)
141 (5.5%)
D
Mitochondrial GO Enrichment - Upregulated Genes in Different conditions
GO Terms
response to oxidative stress
release of cytochrome c from mitochondria
regulation of mitochondrial membrane permeability
mitochondrial outer membrane
mitochondrial membrane organization
apoptotic mitochondrial changes
MAVS
CoV-2 + MAVS
Gene Count
pvalue
E
CoV-2 + MAVS - mitochondrial membrane organization
Differentially expressed genes (upregulated)
CNP
TOMM40
PMAIP1
PPIF
CHCHD10
p-value & Log2 FC
Log2 fold change
total = 23 variables
F
CoV-2 + MAVS - mitochondrial outer membrane
Differentially expressed genes (upregulated)
MAVS
RSAD2
PMAIP1
PDE2A
PLA2G2A
p-value & Log2 FC
Log2 fold change
total = 33 variables
G
Mitochondrial GO Enrichment - Upregulated Genes in MAVS KO MEFs w.r.t WT MEFs
GO Terms
water-soluble vitamin metabolic process
sulfur compound metabolic process
reactive oxygen species metabolic process
proteinogenic amino acid metabolic process
olefinic compound metabolic process
mitochondrial fragmentation involved in apoptotic process
mitochondrial fission
L-amino acid metabolic process
intrinsic apoptotic signaling pathway in response to oxidative stress
hormone metabolic process
collagen metabolic process
cellular aldehyde metabolic process
apoptotic mitochondrial changes
acetyl-CoA metabolic process
Mock_12h
Infected_12h
Mock_24h
Infected_24h
Mock_48h
Infected_48h
Gene Count
pvalue
H
Mock_48h - mitochondrial fission
Differentially expressed genes (upregulated)
Dcn
Prkn
Pparg
Ppargc1a
Ppp2r2b
Log2 fold change
total = 5 variables
I
Infected_12h - apoptotic mitochondrial changes
Differentially expressed genes (upregulated)
Mmp9
Cck
Pmaip1
Cdkn2a
Ppp2r2b
p-value & Log2 FC
Log2 fold change
total = 6 variables
J
Mitochondrial GO Enrichment - downregulated Genes in MAVS KO MEFs w.r.t WT MEFs
GO Terms
response to oxidative stress
regulation of mitochondrial fission
proton motive force-driven mitochondrial ATP synthesis
positive regulation of mitochondrial fission
oxidative phosphorylation
negative regulation of lipid metabolic process
mitochondrial transport
mitochondrial respiratory chain complex assembly
mitochondrial respirasome
mitochondrial membrane organization
mitochondrial gene expression
inner mitochondrial membrane protein complex
glutathione metabolic process
catecholamine metabolic process
catechol-containing compound metabolic process
ATP metabolic process
Mock_12h
Mock_24h
Infected_24h
Mock_48h
Infected_48h
p.adjust
Gene Count
K
Infected_48h - oxidative phosphorylation
Differentially expressed genes (downregulated)
ND5
ND6
ND4
ND2
ND1
ATP6
ATP8
p-value & Log2 FC
Log2 fold change
total = 12 variables
L
Mock_48h - mitochondrial respirasome
Differentially expressed genes (downregulated)
Ndufs5
ND4L
AA467197
ND6
ND2
p-value & Log2 FC
Log2 fold change
total = 16 variables
M
Mock_12h - mitochondrial membrane organization
Differentially expressed genes (downregulated)
Tomm70a
Hsp90aa1
Bax
Cox18
Timm13
p-value & Log2 FC
Log2 fold change
total = 12 variables
N
Mock_12h - mitochondrial transport
Differentially expressed genes (downregulated)
Tomm70a
Pnpt1
Hspd1
Nptx1
Timm23
p-value & Log2 FC
Log2 fold change
total = 18 variables

Figure 5

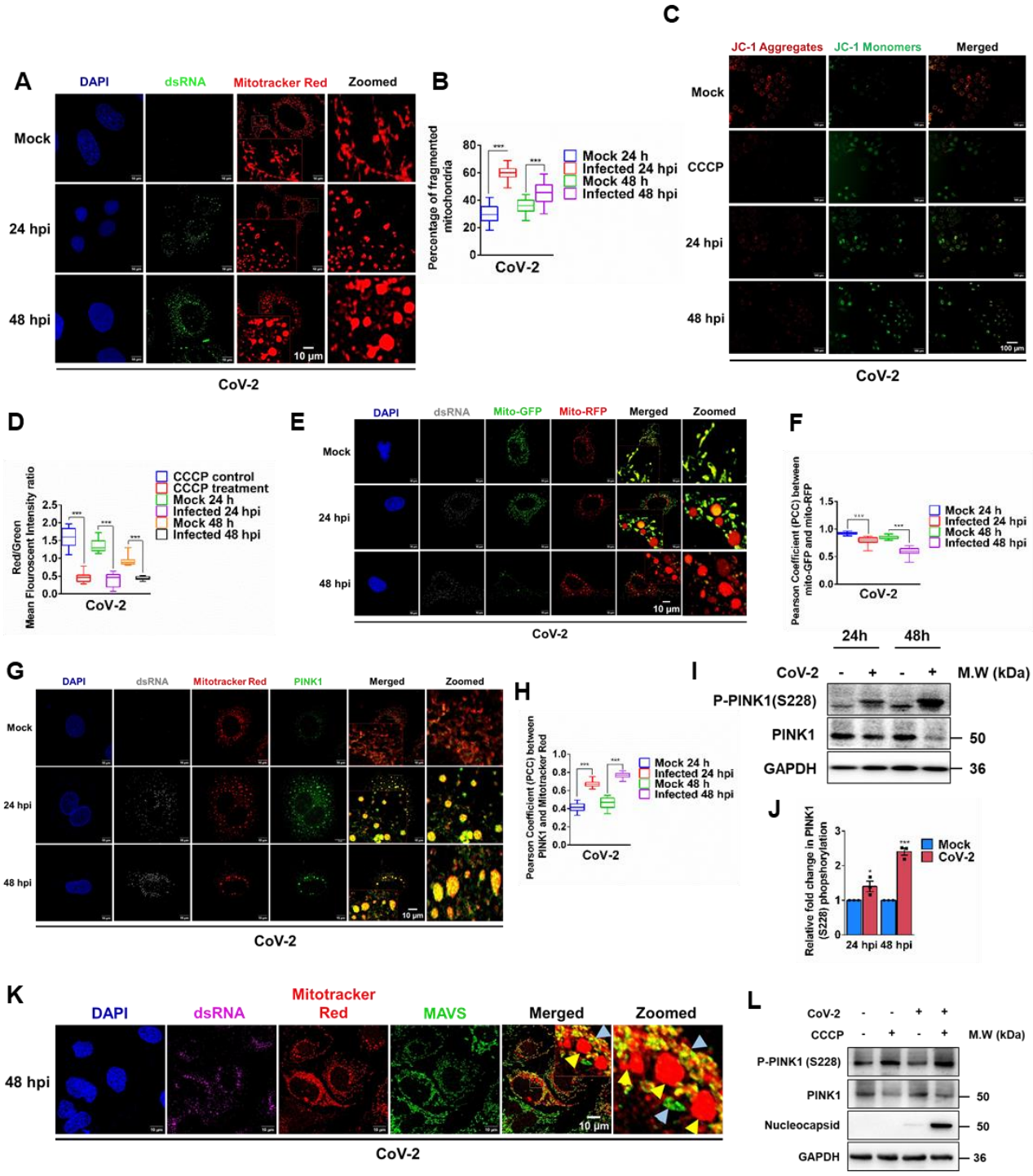
A
DAPI
dsRNA
Mitotracker Red
Zoomed
Mock
24 hpi
48 hpi
10 µm
CoV-2
B
Percentage of fragmented mitochondria
Mock 24 h
Infected 24 hpi
Mock 48 h
Infected 48 hpi
CoV-2
C
JC-1 Aggregates
JC-1 Monomers
Merged
Mock
CCCP
24 hpi
48 hpi
100 µm
CoV-2
D
Red/Green Mean Flouroscent Intensity ratio
CCCP control
CCCP treatment
Mock 24 h
Infected 24 hpi
Mock 48 h
Infected 48 hpi
CoV-2
E
DAPI
dsRNA
Mito-GFP
Mito-RFP
Merged
Zoomed
Mock
24 hpi
48 hpi
10 µm
CoV-2
F
Pearson Coefficient (PCC) between mito-GFP and mito-RFP
Mock 24 h
Infected 24 hpi
Mock 48 h
Infected 48 hpi
CoV-2
24h
48h
G
DAPI
dsRNA
Mitotracker Red
PINK1
Merged
Zoomed
Mock
24 hpi
48 hpi
10 µm
CoV-2
H
Pearson Coefficient (PCC) between PINK1 and Mitotracker Red
Mock 24 h
Infected 24 hpi
Mock 48 h
Infected 48 hpi
CoV-2
I
CoV-2
M.W (kDa)
P-PINK1(S228)
PINK1
GAPDH
50
36
J
Relative fold change in PINK1 (S228) phopshorylation
Mock
CoV-2
24 hpi 48 hpi
K
DAPI
dsRNA
Mitotracker Red
MAVS
Merged
Zoomed
48 hpi
10 µm
CoV-2
L
CoV-2
CCCP
M.W (kDa)
P-PINK1 (S228)
PINK1
Nucleocapsid
GAPDH
50
50
36
M
Relative fold change in Nucleocapsid expression
CoV-2
CoV-2 + CCCP
N
Relative fold change in PINK1 (S228) phopshorylation
Mock
Mock + CCCP
CoV-2
CoV-2 + CCCP
O
PFU/mL (log)
CoV-2
CoV-2 + CCCP

1153 **Figure 6**

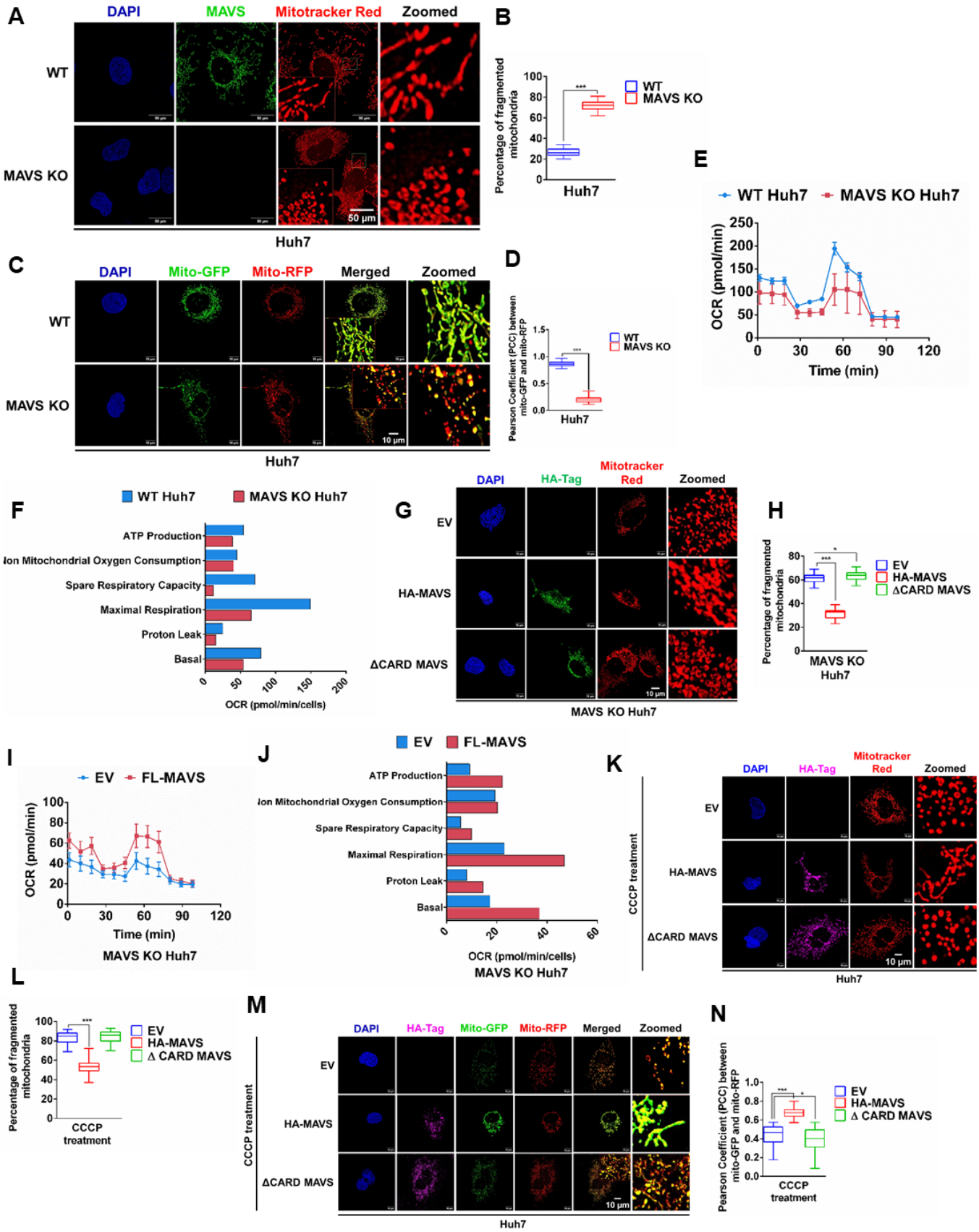

1154

1155 **Figure 7**

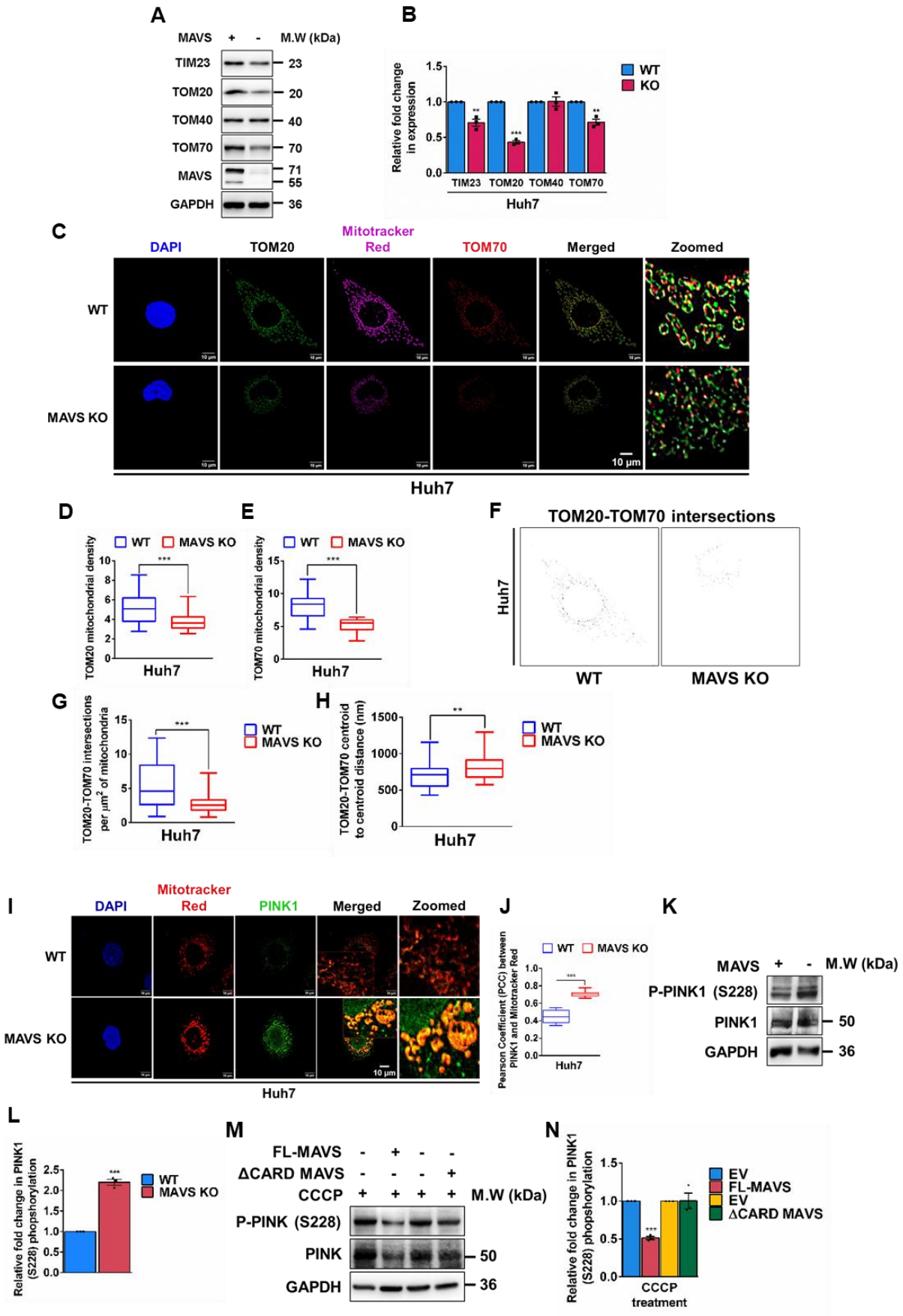

1156

Figure 8

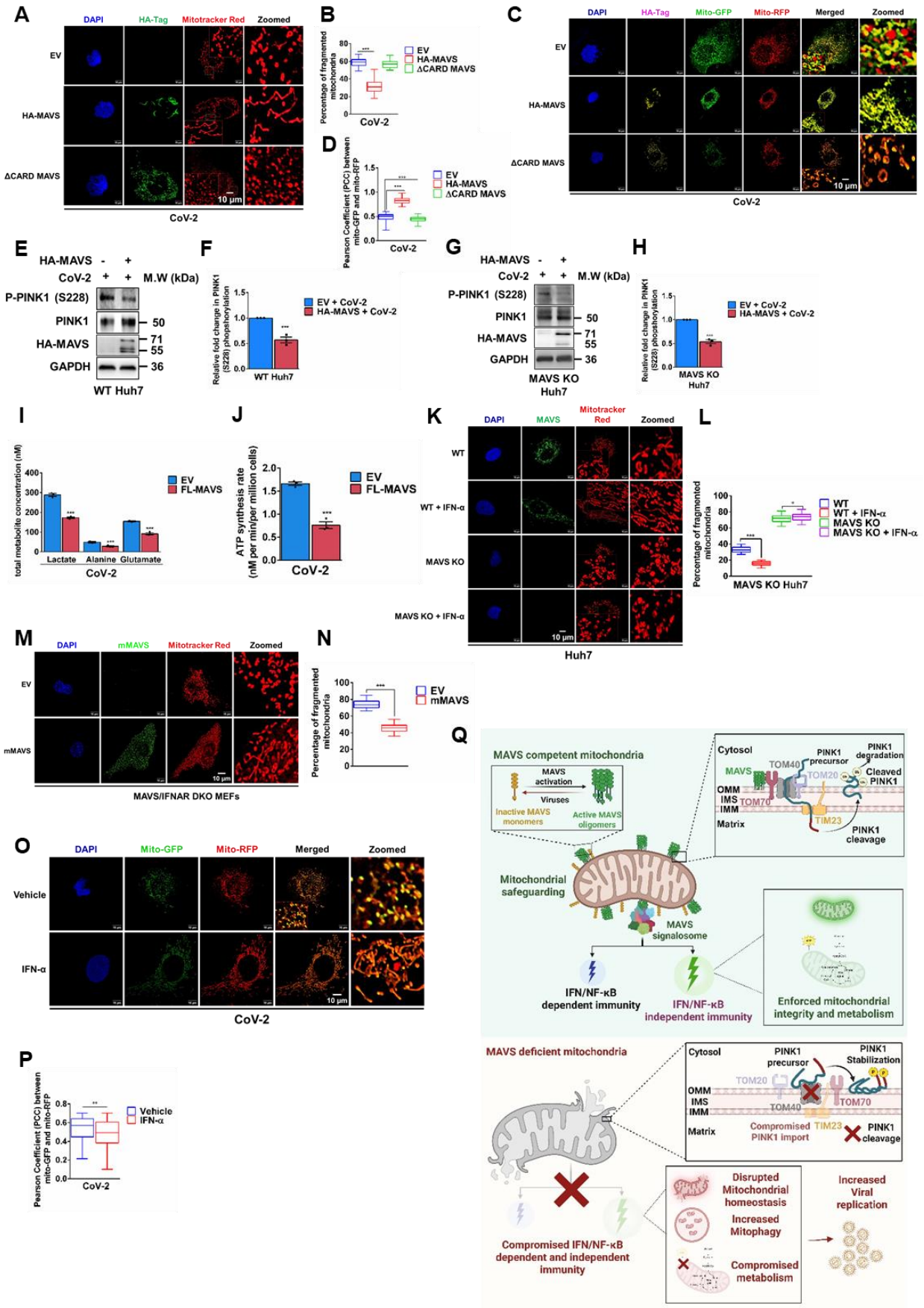
A
DAPI
HA-Tag
Mitotracker Red
Zoomed
EV
HA-MAVS
ΔCARD MAVS
10 µm
CoV-2
B
Percentage of fragmented mitochondria
EV
HA-MAVS
ΔCARD MAVS
CoV-2
C
DAPI
HA-Tag
Mito-GFP
Mito-RFP
Merged
Zoomed
EV
HA-MAVS
ΔCARD MAVS
10 µm
CoV-2
D
Pearson Coefficient (PCC) between mito-GFP and mito-RFP
EV
HA-MAVS
ΔCARD MAVS
CoV-2
E
HA-MAVS - +
CoV-2 + +
M.W (kDa)
P-PINK1 (S228)
PINK1
HA-MAVS
GAPDH
50
71
55
36
WT Huh7
F
Relative fold change in PINK1 (S228) phosphorylation
EV + CoV-2
HA-MAVS + CoV-2
WT Huh7
G
HA-MAVS - +
CoV-2 + +
M.W (kDa)
P-PINK1 (S228)
PINK1
HA-MAVS
GAPDH
50
71
55
36
MAVS KO Huh7
H
Relative fold change in PINK1 (S228) phosphorylation
EV + CoV-2
HA-MAVS + CoV-2
MAVS KO Huh7
I
total metabolite concentration (nM)
EV
FL-MAVS
Lactate
Alanine
Glutamate
CoV-2
J
ATP synthesis rate (nM per min/per million cells)
EV
FL-MAVS
CoV-2
K
DAPI
MAVS
Mitotracker Red
Zoomed
WT
WT + IFN-α
MAVS KO
MAVS KO + IFN-α
10 µm
Huh7
L
Percentage of fragmented mitochondria
WT
WT + IFN-α
MAVS KO
MAVS KO + IFN-α
MAVS KO Huh7
M
DAPI
mMAVS
Mitotracker Red
Zoomed
EV
mMAVS
10 µm
MAVS/IFNAR DKO MEFs
N
Percentage of fragmented mitochondria
EV
mMAVS
Q
MAVS competent mitochondria
MAVS activation
Viruses
Inactive MAVS monomers
Active MAVS oligomers
Cytosol
MAVS
TOM40
PINK1 precursor
PINK1 degradation
TOM20
Cleaved PINK1
OMM
IMS
IMM
TOM70
Matrix
TIM23
PINK1 cleavage
Mitochondrial safeguarding
MAVS signalosome
IFN/NF-κB dependent immunity
IFN/NF-κB independent immunity
Enforced mitochondrial integrity and metabolism
MAVS deficient mitochondria
Cytosol
PINK1 precursor
PINK1 Stabilization
TOM20
OMM
IMS
IMM
TOM40
TOM70
Matrix
Compromised PINK1 import
TIM23
PINK1 cleavage
Compromised IFN/NF-κB dependent and independent immunity
Disrupted Mitochondrial homeostasis
Increased Mitophagy
Compromised metabolism
Increased Viral replication
O
DAPI
Mito-GFP
Mito-RFP
Merged
Zoomed
Vehicle
IFN-α
10 µm
CoV-2
P
Pearson Coefficient (PCC) between mito-GFP and mito-RFP
Vehicle
IFN-α
CoV-2

LEGENDS

Figure 1. CoV-2 disrupts MAVS aggregation and evades the RLR-mediated Immunity

(A) SDD-AGE showing MAVS aggregation in CoV-2 infected Huh7 cells at indicated time points, compared to uninfected controls. **(B)** Confocal images showing MAVS aggregation in Huh7 cells infected with CoV-2, stained with Mitotracker Red and immunostained for dsRNA and MAVS. **(C)** Quantification of Pearson's correlation coefficient (PCC) for MAVS-mitochondria co-localization from (B) (n = 250 ROIs). **(D-E)** Immunoblots analyzing IRF3 phosphorylation and CoV-2 nucleocapsid levels in Huh7 cells overexpressing RIG-I, MDA5, or HA-TBK1, following infection. **(F)** Densitometric quantification of IRF3 phosphorylation from (D-E). **(G)** qRT-PCR analysis of *IFNB1* mRNA levels from (D-E). **(H)** Infectious viral titers upon RIG-I and MDA5 overexpression in infected Huh7 cells. **(I)** Immunoblot of IRF3 phosphorylation and nucleocapsid expression in cells overexpressing HA-IRF3 (WT) or IRF3 S396E mutant after CoV-2 infection. **(J)** qRT-PCR analysis of *IFNB1* and **(K)** CoV-2 RNA levels from (I). Scale bars, 10 µm unless otherwise indicated.

Figure 2. Functional MAVS can efficiently restrict CoV-2

(A) Immunoblot showing HA-MAVS and CoV-2 nucleocapsid levels in Huh7 cells overexpressing HA-tagged FL-MAVS or ΔCARD MAVS after CoV-2 infection. **(B)** Infectious viral titers from corresponding supernatants. **(C)** Confocal images detecting dsRNA in similarly treated cells, and **(D)** quantification of dsRNA mean fluorescence intensity (MFI) (n = 50 cells). **(E)** Immunoblot showing MAVS and CoV-2 nucleocapsid levels in WT and MAVS KO Huh7 cells following infection, and **(F)** corresponding infectious viral titers. **(G)** Confocal images and **(H)** quantification of dsRNA intensity in samples from (E) (n = 100 cells). **(I)** Confocal images showing dsRNA in MAVS KO Huh7 cells transfected with HA-tagged FL-MAVS or ΔCARD MAVS and infected with CoV-2, and **(J)** dsRNA intensity quantification (n = 100 cells). **(K)** Infectious titers from corresponding supernatants. **(L)** Immunoblot showing ACE2 levels across different cell types. **(M)** Immunoblot analysing MAVS expression and CoV-2 nucleocapsid levels in WT and MAVS KO A549 cells infected with CoV-2. **(N)** Infectious titers comparing CoV-2 infection in WT and MAVS KO A549 cells. **(O)**

Immunoblot analysing CoV-2 nucleocapsid levels in WT and MAVS KO MEFs infected with CoV-2. **(P)** Infectious viral titers comparing infection in WT and MAVS KO MEFs. Scale bars, 10 µm unless otherwise indicated.

Figure 3. The antiviral effect of MAVS against CoV-2 is independent of type I and type III IFN, and NF-κB signaling

(A) Immunoblot analyzing IRF3 phosphorylation in CoV-2 infected Huh7 cells overexpressing FL-MAVS or ΔCARD MAVS. **(B)** Densitometric analysis of IRF3 phosphorylation. **(C)** qRT-PCR analysis of *IFNB1* mRNA levels and **(D)** ELISA for IFN-α from corresponding supernatants. **(E)** Relative fold change in infectious viral titers upon MAVS overexpression in Huh7 cells infected with different CoV-2 variants. **(F)** qRT-PCR analysis of *IFNL1* mRNA levels from (A). **(G)** Immunoblot showing STAT1 phosphorylation, CoV-2 nucleocapsid, and HA-MAVS levels in IFN-λ-treated, CoV-2-infected Caco2 cells, and **(H)** nucleocapsid expression levels. **(I)** qRT-PCR of CoV-2 RNA from (G). **(J)** Immunoblot analyzing STAT1 phosphorylation, CoV-2 nucleocapsid, and HA-MAVS levels in CoV-2 infected Huh7 cells overexpressing MAVS, treated with IFN-α, or both, and **(K)** infectious viral titers from corresponding supernatants. **(L)** Immunoblot showing STAT1 phosphorylation, IFIT1, HA-MAVS, and nucleocapsid levels in Huh7 cells overexpressing MAVS, treated with Baricitinib, or their combination, and **(M)** corresponding viral titers. **(N)** Immunoblot showing STAT1 phosphorylation, HA-MAVS, and nucleocapsid levels in Huh7 cells treated with type I IFN neutralizing antibodies, and **(O)** viral titers. **(P)** Immunoblot showing mMAVS and nucleocapsid expression in CoV-2 infected MAVS:IFNAR DKO MEFs, and **(Q)** infectious viral titers. **(R)** Immunoblot showing p65 phosphorylation, MAVS, and nucleocapsid levels in Huh7 cells overexpressing MAVS or treated with BAY11-7082, and **(S)** infectious viral titers.

Figure 4. MAVS regulates a broader transcriptional landscape, distinct from IFN

(A) Heatmap showing differentially expressed genes (DEGs) upon MAVS overexpression or IFN-α treatment in uninfected and CoV-2 infected Huh7 cells, represented as $\log_2$ fold changes. **(B-C)** Venn diagrams showing DEG overlap between MAVS overexpression and IFN-α treatment in (B) uninfected and (C) CoV-2

infected conditions. **(D)** Dot plot of Gene Ontology (GO) enrichment for upregulated mitochondrial processes in MAVS and CoV-2 + MAVS conditions. **(E-F)** Enhanced volcano plots showing upregulated DEGs related to (E) mitochondrial membrane organization and (F) mitochondrial outer membrane during CoV-2 infection in Huh7 cells; upregulated genes labelled in green. **(G)** GO enrichment dot plot for upregulated mitochondrial processes in uninfected and CoV-2 infected MAVS KO MEFs compared to WT MEFs. **(H-I)** Enhanced volcano plots showing DEGs related to (H) mitochondrial fission and (I) apoptotic mitochondrial changes at different time points in mock or CoV-2 infected MEFs; upregulated genes labelled in green. **(J)** Dot plot showing GO enrichment for downregulated mitochondrial processes in MAVS KO MEFs. **(K-N)** Enhanced volcano plots of DEGs related to (K) oxidative phosphorylation, (L) mitochondrial respirasome, (M) mitochondrial membrane organization, and (N) mitochondrial transport; downregulated genes labelled in red.

Figure 5. CoV-2 disrupts mitochondrial homeostasis and causes mitophagy that benefits its replication

(A) Confocal images showing mitochondrial fragmentation in CoV-2 infected Huh7 cells. **(B)** Quantification of mitochondrial fragmentation from (A). **(C)** Epifluorescence microscopy images analyzing mitochondrial membrane potential at different time points post-CoV-2 infection (MOI = 1), with CCCP as a positive control. **(D)** Quantification of mitochondrial membrane potential from (C) (n = 100 cells). Scale bars, 100 µm. **(E)** Confocal images showing mitophagy in CoV-2 infected Huh7 cells transfected with a Mito-GFP-RFP reporter, and **(F)** corresponding quantification. **(G)** Confocal images showing PINK1 (green) co-localization with MitoTracker Red (red) in infected cells, and **(H)** quantification of PINK1 localization. **(I)** Immunoblot analyzing PINK1 phosphorylation (S228) in CoV-2 infected Huh7 cells, and **(J)** densitometric quantification. **(K)** Confocal images showing exclusion of MAVS from fragmented mitochondria in Huh7 cells infected for 48 h; yellow arrows denote mitochondria lacking MAVS, blue arrows indicate mitochondria with intact MAVS. **(L)** Immunoblot analyzing PINK1 phosphorylation following CCCP treatment in uninfected or CoV-2 infected Huh7 cells. **(M)** Densitometric analysis of CoV-2 nucleocapsid levels and **(N)** PINK1 phosphorylation from (L). **(O)** Infectious viral

titers from corresponding supernatants. Scale bars, 10 µm and n = 50 cells unless otherwise indicated.

Figure 6. MAVS deficiency predisposes mitochondria to mitophagy and dysfunction

(A) Confocal images showing mitochondrial fragmentation in Huh7 WT and MAVS KO cells, and **(B)** corresponding quantification. Scale bars, 50 µm. **(C)** Confocal images showing mitophagy in Huh7 WT and MAVS KO cells transfected with a Mito-GFP-RFP reporter, and **(D)** corresponding quantification. **(E)** Oxygen consumption rate (OCR) and **(F)** mitochondrial respiration parameters in WT and MAVS KO Huh7 cells measured by Mito Stress Assay and analyzed using the Seahorse XFe24 analyzer. **(G)** Confocal images showing mitochondrial fragmentation in MAVS KO Huh7 cells transfected with FL-MAVS or ΔCARD MAVS, and **(H)** corresponding quantification. **(I)** OCR and **(J)** mitochondrial respiration parameters in MAVS KO cells transfected with FL-MAVS. **(K)** Confocal images showing mitochondrial fragmentation in CCCP-treated Huh7 cells overexpressing FL-MAVS or ΔCARD MAVS, and **(L)** corresponding quantification. **(M)** Confocal images showing mitophagy in CCCP-treated Huh7 cells overexpressing FL-MAVS or ΔCARD MAVS, along with a Mito-GFP-RFP reporter, and **(N)** corresponding quantification. Scale bars, 10 µm and n = 50 cells unless otherwise indicated.

Figure 7. MAVS supports mitochondrial protein import machinery/complex and restricts PINK1-mediated mitophagy

(A) Immunoblot analysis of TIM23, TOM20, TOM40, TOM70, and MAVS levels in Huh7 WT and MAVS KO cells, and **(B)** corresponding quantification. **(C)** Confocal images showing co-localization of TOM20 and TOM70 puncta in WT and MAVS KO Huh7 cells. **(D)** Intersection masks highlighting TOM20 and TOM70 overlaps, and **(E)** quantification of intersection density per unit mitochondrial area. **(F)** Quantification of centroid-to-centroid distances between TOM20 and TOM70 in WT and MAVS KO cells. **(G)** Confocal images showing co-localization of PINK1 (green) with Mitotracker Red (red) in WT and MAVS KO cells, and **(H)** corresponding quantification. **(I)** Immunoblot analysis of PINK1 phosphorylation in WT and MAVS KO cells, and **(J)** densitometric quantification. **(K)** Immunoblot analysis of PINK1

phosphorylation in CCCP-treated Huh7 cells expressing FL-MAVS or ΔCARD MAVS, and **(L)** corresponding quantification. Scale bars, 10 µm and n = 50 cells.

Figure 8. MAVS protects mitochondria from virus-induced damage and mediates IFN-independent antiviral immunity

(A) Confocal images analyzing mitochondrial fragmentation in CoV-2 infected Huh7 cells overexpressing HA-tagged FL-MAVS or ΔCARD-MAVS, and **(B)** corresponding quantification. **(C)** Confocal images analyzing mitophagy in similarly treated cells, and **(D)** corresponding quantification. **(E)** Immunoblot analysis of PINK1 phosphorylation in CoV-2 infected Huh7 WT cells overexpressing FL-MAVS, and **(F)** densitometric quantification. **(G)** Immunoblot analysis of PINK1 phosphorylation in CoV-2 infected Huh7 MAVS KO cells overexpressing FL-MAVS, and **(H)** corresponding quantification. **(I)** Quantification of total glycolytic metabolite levels and **(J)** ATP synthesis rates by 1D metabolic NMR in CoV-2 infected Huh7 cells overexpressing FL-MAVS. **(K)** Confocal images analyzing mitochondrial fragmentation in IFN-α treated Huh7 WT and MAVS KO cells, and **(L)** corresponding quantification. **(M)** Confocal images showing mitochondrial fragmentation in MAVS/IFNAR DKO MEFs overexpressing mMAVS, and **(N)** corresponding quantification. **(O)** Confocal images showing mitophagy in CoV-2 infected, IFN-α treated Huh7 cells, and **(T)** corresponding quantification. **(Q)** Schematic model for MAVS mediated antiviral protection via mitochondrial safeguarding. Scale bars, 10 µm and n = 50 cells.